Eur. Phys. J. B **24**, 267–284 (2001)

THE EUROPEAN PHYSICAL JOURNAL B

EDP Sciences

Polarizability of truncated spheroidal particles supported by a substrate: model and applications

R. Lazzari[1], I. Simonsen[1,2], D. Bedeaux[3], J. Vlieger[3], and J. Jupille[1,a]

[1] Laboratoire Mixte CNRS/Saint-Gobain "Surface du Verre et Interfaces" 39, Quai Lucien Lefranc, BP 135, 93303 Aubervilliers Cedex, France
[2] Department of Physics, The Norwegian University of Science and Technology, 7491 Trondheim, Norway
[3] Leiden Institut of Chemistry, Leiden University PO Box 9502, 2300 RA Leiden, The Netherlands

Received 5 June 2000 and Received in final form 31 July 2001

Abstract. The light scattering by three-dimensional clusters supported by a substrate is modelled by representing clusters by truncated spheroids whose polarizability is calculated *via* a multipolar development of the potential in the quasi-static limit. The determination of the mean island radius, density and aspect ratio from the optical response is examined. The strong influence of both the particle-substrate interaction and the particle shape on the optical behaviour is demonstrated, showing the limits of effective medium and dipolar theories. The Surface Differential Reflectance spectra of silver on MgO(100) and titanium or aluminium on α-Al_2O_3(0001) surfaces have then been modelled by using the above model, illustrating the capability of optical means to deal with various metals, including those belonging to transition series. In all cases, it is highlighted that the aspect ratio is central in modelling the optical response of supported particles.

PACS. 78.20.Bh Theory, models, and numerical simulation – 73.20.Mf Collective excitations (including excitons, polarons, plasmons and other charge-density excitations) – 68.55.Ac Nucleation and growth: microscopic aspects

1 Introduction

Light scattering from small particles is at the origin of many colors effects in nature and affects many reflection-transmission-absorption behaviours. For those reasons, it has received a tremendous attention in the past four decades, both experimentally and theoretically [1], in particular for silver and alkali metals whose behaviour is accurately accounted for by means of the free-electron gas theory. Light scattering offers elegant and non-destructive means to probe particles in very versatile conditions of environment in either vacuum, gas or transparent liquid. In particular, for the study of supported aggregates during either chemical vapor deposition or metal deposition, Surface Differential Reflectance (SDR) has proved to allow for an *in situ* and in real time characterization of the cluster size, density and aspect ratio *via* high quality optical spectra, even within the submonolayer range [2–4].

The crucial point is to unambiguously identify the spectral features and to quantitatively interpret the optical data. The effective medium theories, such as Maxwell Garnett or Bruggeman model, fail to describe the experimental spectra in details. Indeed, they assume a strongly simplified picture for the supported particles. In particular, the interaction with the substrate is treated by embedding the particle in an effective medium whose dielectric constant is between that of vacuum and that of the substrate. Yamaguchi *et al.* [5,6] have first set up an approach including the substrate-induced breaking of symmetry. In their model, each particle is replaced by a point-dipole and its electrostatic image in the substrate. The renormalized polarizability is then obtained by summing the contributions of all the local fields of neighbours and images. However, this description does neither account for the shape of the particle nor for the multipolar coupling with the substrate, which have both been shown to dramatically affect the optical response of supported clusters.

A more sophisticated picture of interacting supported particles can be achieved by means of the theoretical approach of the Fresnel coefficients of a thin film which has been developed by Bedeaux and Vlieger [7–12]. The thin film is represented by a boundary layer lying between two bulk media whose thickness is supposed to be small enough with respect to the wavelength of light for the non-retarded limit to hold. The optical response of this layer is treated by bringing back to the surface, as Dirac terms, all the integrated excess fields from the simple

[a] e-mail: Jacques.Jupille@saint-gobain.com

Fresnel behaviour. The surface being non-magnetic, four coefficients, called surface susceptibility, γ_e, β_e, τ and δ are introduced. The reflection and transmission amplitudes, the ellipsometric coefficients can be expressed in terms of these parameters. The susceptibilities γ, which gives the integrated surface polarization parallel to the surface in term of the electric field along the surface, and β, which relates the integrated surface polarization normal to the surface in terms of the electric displacement field normal to the surface are given as functions of the exact local dielectric constant $\epsilon(z)$ along z by:

$$\gamma_e = \int_{-\infty}^{+\infty} [\epsilon(z) - \epsilon^- \theta(-z) - \epsilon^+ \theta(z)] \mathrm{d}z, \qquad (1.1)$$

$$\beta_e = -\int_{-\infty}^{+\infty} [\frac{1}{\epsilon(z)} - \frac{1}{\epsilon^-}\theta(-z) - \frac{1}{\epsilon^+}\theta(z)] \mathrm{d}z, \quad (1.2)$$

where $\theta(z)$ is the Heaviside function and ϵ^+ and ϵ^- are the dielectric functions of the two surrounding media. There is a clear connection with the non local dielectric tensor introduced by Barrera *et al.* [13] for the description of the anisotropic response of a metallic surface in the jellium approximation. The others coefficients τ and δ, which are of second order with respect to the ratio between the thickness of the layer and the wavelength, can be neglected herein. The parameters γ and β are related to the islands polarizabilities parallel and perpendicular to the surface. All the measurable quantities are independent of the choice of the dividing surface so that invariant combinations of them can be introduced as suggested first by Lekner [7,14]. The calculation mostly consists in determining the island polarizability by accounting for all the above-mentioned interactions.

The choice for the particle geometry was currently limited to that of truncated spheres on a substrate [15–17]. However, the model could hardly be run for high aspect ratio, *i.e.* for spherical caps, because of matrix conditioning [15]. Although this geometry offers a realistic representation of the particles at thermodynamic equilibrium, it does not allow to picture neither partial wetting nor growth modes dominated by kinetics [18]. It is anticipated that a much greater variety of thin films could be represented by approximating particles by truncated spheroids. The aim of the paper is to calculate the polarizability of such objects and to illustrate the capability of the method to deal with experimental cases. The paper is organized as follows. Section 2 is dealing with the calculation of the polarizability of an isolated particle in interaction with the substrate *via* a spheroidal expansion of the potentials. The expansion coefficients which are then determined can be related to measurable quantities which characterize the optical response. In Section 3 the formalism is applied to differential reflectivity spectra collected *in situ* during the formation of thin films in the cases of silver on MgO(100), and titanium or silver on α-Al_2O_3(0001).

2 Polarizability of a truncated spheroid

Truncated spheroids, either prolate or oblate, that are symmetric around an axis of revolution normal to the surface of the substrate with its centre either above (island) or below (cap) the substrate, are depicted in Figure 1. The reason to distinguish between islands and caps lies in the expression of the potentials. The symmetry of the problem implies the use of spheroidal coordinates (ξ, η, ϕ) [19] defined in more details in Appendix A. It is convenient to locate the origin $\mathcal{O}$ for this spheroidal coordinate system at the centre of the spheroid. In addition, an other spheroidal coordinate system (ξ', η', ϕ'), whose origin $\mathcal{O}'$ is at the image point of the centre of the spheroid with respect to the surface of the substrate, is introduced. The appropriate changes of variables between these two systems, as well as with the Cartesian system, are given in Appendix A. The Cartesian system $\mathcal{S}$ has its origin $\mathcal{O}$ at the centre of the spheroid with the z-axis pointing downwards into the substrate. The quantity a stands for the radius of the ring of foci. The surface of the spheroid corresponds to $\xi = \xi_0$ whereas $z = a\xi\eta = \pm d = \pm a\xi_1$ defines the surface of the substrate (+ for an island and − for a cap) which separates the vacuum (medium 1) from the substrate (medium 2) and supports the particle (medium 3). For calculation convenience, the buried part of the particle appears as a different medium 4. The limits in spheroidal coordinates of the various domains are given in Appendix A. A dielectric constant $\epsilon_i(\omega)$ is assigned to each medium ($i = 1, 2, 3, 4$).

Several parameters are used to characterize the shape of the particle and its position with respect to the substrate. The *axial ratio*, $a_r = R_\parallel / R_\perp$, of the spheroid is the ratio of the parallel radius ($R_\parallel$) over the normal radius ($R_\perp$). A useful quantity which maps all the possible axial ratios onto the interval $[0, 1]$ is defined by $x = 1/(1 + a_r)$. The *truncation parameter* t_r is defined by:

$$t_r = \frac{d}{R_\perp} = \frac{d}{a\xi_0} \qquad \text{with} \qquad 0 \le t_r \le 1 \qquad (2.1)$$

where $R_\perp$ is the radius along the surface normal ($R_\perp = R_s, R_l$ for oblate or prolate particle) and d is the distance from the centre of the spheroid to the surface of the substrate. In all formulae, t_r is defined as a positive number. However, in figures, to clarify the presentation of data, negative values of t_r are associated with the spheroidal cap case. For example, $t_r = -1$ describes a completely buried particle. Finally, the *aspect ratio*, s_r, is defined as the cluster diameter seen from above (as in most of the experimental diameter determinations by microscopy techniques) divided by its height $h = R_\perp(1 \pm t_r)$, *i.e.*:

$$s_r = \begin{cases} \dfrac{2a_r}{1 + t_r} & \text{island,} \\ 2a_r\sqrt{\dfrac{1 + t_r}{1 - t_r}} & \text{cap.} \end{cases} \qquad (2.2)$$

The isovalues of s_r in logarithmic scale are presented in Figure 2, where the various regions for oblate or prolate island or cap are indicated.

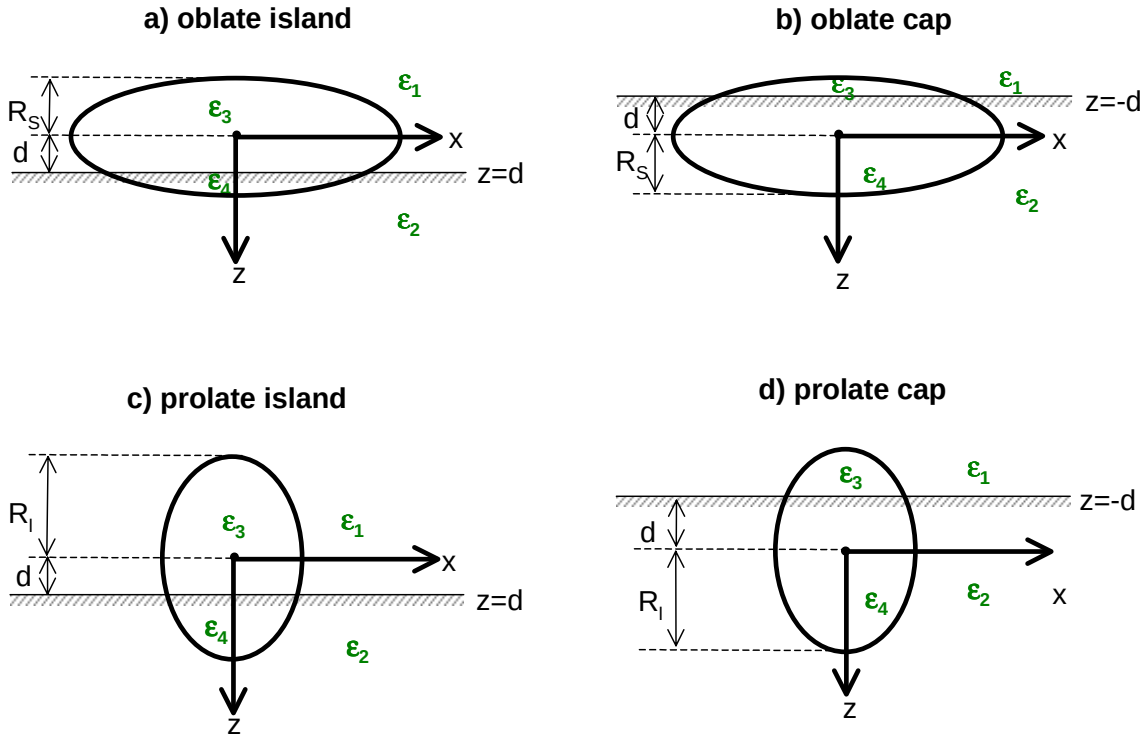

Fig. 1. Cross-sections of the various geometries for truncated spheroidal islands: (a) oblate island (b) oblate cap (c) prolate island (d) prolate cap.

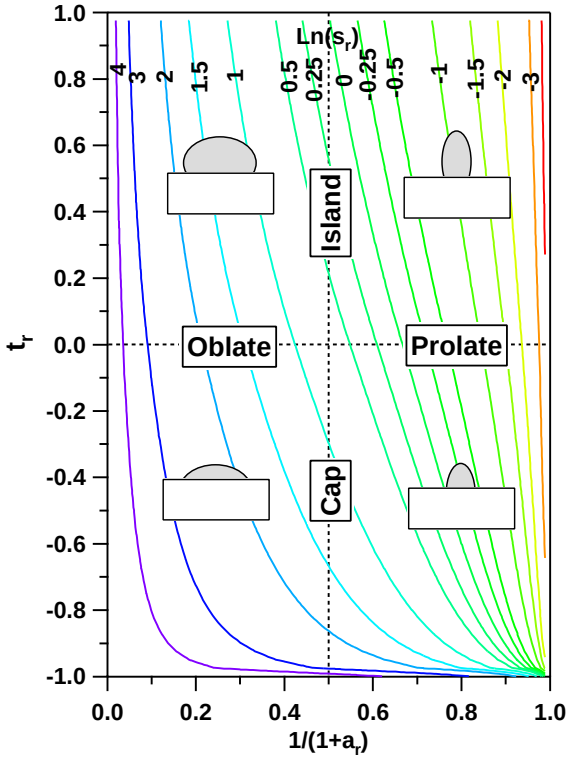

Fig. 2. Isovalues in logarithmic scale for the aspect ratio s_r of the particle, *i.e.* the cluster diameter seen from above divided by its height. The high aspect ratios correspond to oblate particles whereas the low values correspond to prolate particles.

2.1 The Laplace equation and the spheroidal potential expansion

The particle is submitted to an incident plane wave $\mathbf{E}_\mathrm{ext} = \mathbf{E}_0\,\mathrm{e}^{\,\mathrm{i}(\mathbf{k}\cdot\mathbf{r}-\omega t)}$ where $k = 2\pi/\lambda$ is the wave vector, ω the frequency of the incident light and E_0 the field modulus. The central hypothesis of the model presented herein is that the size of the islands are much smaller than the incident wavelength λ, so that all retardation effects can be neglected. The applied field is thus expressed in the electrostatic limit of the Maxwell equations by the potential $\Psi_\mathrm{ext}(\mathrm{r},\mathrm{t}) \equiv -\mathbf{E}_0\cdot\mathbf{r}\,\mathrm{e}^{\,-\mathrm{i}\omega\mathrm{t}}$. For charge-free clusters made of non-magnetic materials, the total (applied plus induced) electric potential $\Psi(\mathbf{r})$ in all four media can thus be derived from the Laplace equation:

$$\nabla^2\Psi(\mathbf{r}) = 0 \qquad \text{with} \qquad \mathbf{E}(\mathbf{r}) = -\nabla\Psi(\mathbf{r}). \tag{2.3}$$

In spheroidal coordinates, the potential is separable into two types of function which both satisfy the Laplace equation and can be written in the form of a product of spheroidal harmonics and "radial" (ξ) functions [19]:

$$\Psi(\mathbf{r}) = \sum_{\ell m} A_{\ell m} Z_\ell^m(\xi,a) Y_\ell^m(\arccos\eta,\phi) + \sum_{\ell m} B_{\ell m} X_\ell^m(\xi,a) Y_\ell^m(\arccos\eta,\phi). \tag{2.4}$$

The summation is from $\ell = 0$ to ∞ and $m = -\ell$ through ℓ. The expansion (2.4) is known as a *spheroidal multipolar expansion* of the potential [19]. Here $A_{\ell m}$ and $B_{\ell m}$ are unknown expansion coefficients and the functions $X_\ell^m(\xi, a)$, $Z_\ell^m(\xi, a)$ and $Y_\ell^m(\arccos\eta, \phi)$ are defined in Appendix B. Multipolar coefficients associated with the reflected and transmitted field will be denoted by superscripts r and t, respectively. Notice that the X_ℓ^m and Z_ℓ^m functions show different asymptotic behaviours (Eqs. (B10)).

2.1.1 Potential expansion for the oblate island with its centre above the surface

The potential expansion for an oblate island is obtained by placing multipoles at the centre of the spheroid $\mathcal{O}$ and at its mirror image $\mathcal{O}'$. The potential in vacuum (region 1) takes the following form:

$$\Psi_1(\mathbf{r}) = \Psi_{\text{ext}}(\mathbf{r}) + {\sum_{\ell m}}' A_{\ell m}\widehat{Z}_\ell^m(\xi, a)Y_\ell^m(\arccos\eta, \phi) + {\sum_{\ell m}}' A_{\ell m}^r\widehat{Z}_\ell^m(\xi', a)Y_\ell^m(\arccos\eta', \phi), \quad (2.5a)$$

where the first sum accounts for the charge distribution located in the cluster at $\mathcal{O}$ and the other sum for the image charge at $\mathcal{O}'$. The prime superindex in the sums means that $\ell \neq 0$, a consequence of the fact that the system is charge-free. The quantity:

$$\Psi_{\text{ext}}(\mathbf{r}) = V_1^0\widehat{X}_1^0(\xi, a)Y_1^0(\arccos\eta, \phi) + V_1^1\widehat{X}_1^1(\xi, a)Y_1^1(\arccos\eta, \phi) - V_1^{-1}\widehat{X}_1^{-1}(\xi, a)Y_1^{-1}(\arccos\eta, \phi) \quad (2.5b)$$

denotes the potential generated by the uniform applied electric field $\mathbf{E}_0 = E_0(\sin\theta_0, 0, \cos\theta_0)$, with:

$$V_1^0 = -\sqrt{\frac{4\pi}{3}}E_0\cos\theta_0, \qquad V_1^1 = \sqrt{\frac{2\pi}{3}}E_0\sin\theta_0, \qquad V_1^{-1} = -\sqrt{\frac{2\pi}{3}}E_0\sin\theta_0. \quad (2.5c)$$

The potential in the substrate (region 2) is:

$$\Psi_2(\mathbf{r}) = \psi_2' + \Psi_{\text{ext}}^t + {\sum_{\ell m}}' A_{\ell m}^t\widehat{Z}_\ell^m(\xi, a)Y_\ell^m(\arccos\eta, \phi) \quad (2.5d)$$

where ψ_2' is a constant. The constant potential Ψ_{ext}^t, corresponding to the transmitted field, is in the same form as $\Psi_{\text{ext}}(\mathbf{r})$ except that the quantities V_1^k are replaced by three constants c_1, c_2, and c_3 to be determined. Furthermore, the potentials in region 3 (island) and region 4 can be written in the following form:

$$\Psi_3(\mathbf{r}) = \psi_3' + {\sum_{\ell m}}' B_{\ell m}\widehat{X}_\ell^m(\xi, a)Y_\ell^m(\arccos\eta, \phi) + {\sum_{\ell m}}' B_{\ell m}^r\widehat{X}_\ell^m(\xi', a)Y_\ell^m(\arccos\eta', \phi), \quad (2.5e)$$

$$\Psi_4(\mathbf{r}) = \psi_4' + {\sum_{\ell m}}' B_{\ell m}^t\widehat{X}_\ell^m(\xi, a)Y_\ell^m(\arccos\eta, \phi), \quad (2.5f)$$

where ψ_3' and ψ_4' are constants.

2.1.2 Potential expansion for the oblate cap

The above expansion of the potential for the oblate island cannot be used in the cap case because the notion of an image point looses its meaning and because the direct field (first sum in Eq. (2.5a)) will not describe correctly the charge distribution in the island [15]. As suggested by Wind *et al.* [16,17], the right expressions are obtained by a permutation of the dielectric constants $\epsilon_1 \leftrightarrow \epsilon_2$, $\epsilon_3 \leftrightarrow \epsilon_4$ with a rotation of the coordinate system used in the potential expansion relative to the island case and a permutation of the transmitted and incident field (see Refs. [7,16,17] for details). The result of that permutation is that the underlying potential is in fact expressed by

$$\Psi_1(\mathbf{r}) = \Psi_{\text{ext}}(\mathbf{r}) + {\sum_{\ell m}}' A_{\ell m}^t\widehat{Z}_\ell^m(\xi, a)Y_\ell^m(\arccos\eta, \phi) \quad (2.6a)$$

$$\Psi_2(\mathbf{r}) = \psi_2' + \psi_{\text{ext}}^t + {\sum_{\ell m}}' A_{\ell m}\widehat{Z}_\ell^m(\xi, a)Y_\ell^m(\arccos\eta, \phi) + {\sum_{\ell m}}' A_{\ell m}^r\widehat{Z}_\ell^m(\xi', \eta), a)Y_\ell^m(\arccos\eta', \phi) \quad (2.6b)$$

$$\Psi_3(\mathbf{r}) = \psi_3' + {\sum_{\ell m}}' B_{\ell m}^t\widehat{X}_\ell^m(\xi, a)Y_\ell^m(\arccos\eta, \phi) \quad (2.6c)$$

$$\Psi_4(\mathbf{r}) = \psi_4' + {\sum_{\ell m}}' B_{\ell m}\widehat{X}_\ell^m(\xi, a)Y_\ell^m(\arccos\eta, \phi) + {\sum_{\ell m}}' B_{\ell m}^r\widehat{X}_\ell^m(\xi', a)Y_\ell^m(\arccos\eta', \phi). \quad (2.6d)$$

Terms with superscripts t and r correspond to multipole fields transmitted from point $\mathcal{O}$ to the ambient (medium 1) and reflected by the substrate, respectively.

For a prolate particle, the expansions are formally the same as for an oblate particle, equations (2.5) and (2.6), except that in all spheroidal functions, the hat is replaced by a tilde, *i.e.* $\widehat{X}_\ell^m \to \widetilde{Z}_\ell^m$ and $\widehat{Z}_\ell^m \to \widetilde{X}_\ell^m$ (Eqs. (B1)).

2.2 Expansion coefficients

The expansions for the potential contain several unknown coefficients like c_i, $A_{\ell m}$, $B_{\ell m}$, etc. which are determined by taking advantage of the boundary conditions at each interface. These are the continuity of the potential itself and of the normal component of the displacement field:

$$\Psi_i(\mathbf{r}_\mathrm{s}) = \Psi_j(\mathbf{r}_\mathrm{s}), \tag{2.7a}$$

$$\epsilon_i(\omega)\,\partial_n\Psi_i(\mathbf{r}_\mathrm{s}) = \epsilon_j(\omega)\,\partial_n\Psi_j(\mathbf{r}_\mathrm{s}). \tag{2.7b}$$

Here, $\mathbf{r}_\mathrm{s}$ is assumed to be any point on the interface and ∂_n denotes the normal derivative.

In the case of an island, the fulfillment of equations (2.7) by the potentials defined in the previous sections on the planar interface outside the island separating medium 1 and 2 leads to:

$$\begin{aligned} &c_1 = -\frac{\epsilon_1}{\epsilon_2}\sqrt{\frac{4\pi}{3}}E_0\cos\theta_0, \qquad c_2 = \sqrt{\frac{2\pi}{3}}E_0\sin\theta_0, \\ &c_3 = -\sqrt{\frac{2\pi}{3}}E_0\sin\theta_0, \qquad \psi_2' = -\left(1-\frac{\epsilon_1}{\epsilon_2}\right) d\; E_0\cos\theta_0, \end{aligned} \tag{2.8}$$

$$A^r_{\ell m} = (-1)^{\ell+m}\left(\frac{\epsilon_1-\epsilon_2}{\epsilon_1+\epsilon_2}\right)A_{\ell m}, \quad A^t_{\ell m} = \frac{2\epsilon_1}{\epsilon_1+\epsilon_2}A_{\ell m}, \tag{2.9}$$

and for the planar interface inside the island separating medium 3 and 4:

$$B^r_{\ell m} = (-1)^{\ell+m}\left(\frac{\epsilon_3-\epsilon_4}{\epsilon_3+\epsilon_4}\right)B_{\ell m}, \qquad B^t_{\ell m} = \frac{2\epsilon_3}{\epsilon_3+\epsilon_4}B_{\ell m}, \tag{2.10}$$

and $\psi_3' = \psi_4' \equiv \psi_0$ where constant potential ψ_0 will be determined later (Eq. (C5)). Notice that the equations for the multipolar coefficients come from the classical multipole-image link [20]. For a cap, the relations are identical except that one should invert the dielectric constants: $\epsilon_1 \leftrightarrow \epsilon_2, \epsilon_3 \leftrightarrow \epsilon_4$ in equations (2.9–2.10) and the sign of ψ_2' in equation (2.8).

From equations (2.9–2.10), it appears that only the two sets $\{A_{lm}\}$ and $\{B_{lm}\}$ of multipolar coefficients are independent. These are determined through the boundary conditions on the surface of the spheroid. By taking advantage of the fact that the spherical harmonics form a complete basis on the spheroidal surface $\xi = \xi_0$, a weak formulation of the boundary conditions can be derived by multiplying equations (2.7) by the complex conjugate spherical harmonic, $[Y_\ell^m(\arccos\eta,\phi)]^*$, and integrating the resulting equations over all angles ($\arccos\eta$ and ϕ):

$$\begin{aligned} &\int_{-1}^{\pm t_\mathrm{r}} \mathrm{d}\eta \int_0^{2\pi} \mathrm{d}\phi (\Psi_1-\Psi_3)_{\xi=\xi_0}[Y_\ell^m(\arccos\eta,\phi)]^* \\ &\quad + \int_{\pm t_\mathrm{r}}^{1} \mathrm{d}\eta \int_0^{2\pi} \mathrm{d}\phi (\Psi_2-\Psi_4)_{\xi=\xi_0}[Y_\ell^m(\arccos\eta,\phi)]^* = 0 \end{aligned} \tag{2.11a}$$

$$\begin{aligned} &\int_{-1}^{\pm t_\mathrm{r}} \mathrm{d}\eta \int_0^{2\pi} \mathrm{d}\phi \left[\frac{\partial}{\partial\xi}(\epsilon_1\Psi_1-\epsilon_3\Psi_3)_{\xi=\xi_0}\right][Y_\ell^m(\arccos\eta,\phi)]^* \\ &\quad + \int_{\pm t_\mathrm{r}}^{1} \mathrm{d}\eta \int_0^{2\pi} \mathrm{d}\phi \left[\frac{\partial}{\partial\xi}(\epsilon_2\Psi_2-\epsilon_4\Psi_4)_{\xi=\xi_0}\right] \\ &\qquad \times [Y_\ell^m(\arccos\eta,\phi)]^* = 0. \end{aligned} \tag{2.11b}$$

The right sign has to be used for t_r (+ for an island and − for a cap). Upon substitution of the expressions for the potentials equations (2.5) and (2.6) into equations (2.11) and using the orthogonality relations for the spherical harmonics, an infinite set of linear equations for the multipolar coefficients is obtained:

$$\sum_{\ell_1=|m|}^{\infty\prime} C^m_{\ell\ell_1}R_\perp^{-\ell_1-2}A_{\ell_1 m} + \sum_{\ell_1=|m|}^{\infty\prime} D^m_{\ell\ell_1}R_\perp^{\ell_1-1}B_{\ell_1 m} = H^m_\ell \tag{2.12a}$$

$$\sum_{\ell_1=|m|}^{\infty\prime} F^m_{\ell\ell_1}R_\perp^{-\ell_1-2}A_{\ell_1 m} + \sum_{\ell_1=|m|}^{\infty\prime} G^m_{\ell\ell_1}R_\perp^{\ell_1-1}B_{\ell_1 m} = J^m_\ell \tag{2.12b}$$

where the system elements $C^m_{\ell\ell_1}$, $D^m_{\ell\ell_1}$, $F^m_{\ell\ell_1}$, $G^m_{\ell\ell_1}$, H^m_ℓ and J^m_ℓ are defined in Appendix C.1. Furthermore $\ell = 0, 1, 2, 3, ...$ and $m = 0, \pm1$, while $R_\perp = a\xi_0$ is the length of the short axis perpendicular to the surface of the substrate. The sums are understood to exclude the $\ell_1 = 0$ term because of the lack of free charge. Notice that the multipolar terms with $|m| \geq 2$ do not couple to the linear incident field and that the equation for $l = 0$, $m = 0$ is useful only to determine the unknown quantity ψ_0. The $m = 0$ system comes from the perpendicular component of the electric field $E_{0,z}$ whereas the $m = \pm1$ cases (degenerated because of the rotational invariance along the $z-$axis) reflect the excitation by $E_{0,x}$ and $E_{0,y}$.

In a complete analogous way (Appendix C.1), a linear system can be derived for an oblate cap. For prolate island and cap, the derivation is similar as above, provided the right interfaces limits and spheroidal functions are used (Eqs. (A7–B1)).

2.3 The surface susceptibilities and the Fresnel coefficients

2.3.1 The polarizability tensor

In the presence of the external field $\mathbf{E}_\mathrm{ext}$, a particle of much smaller size than the wavelength of the incident light is polarized in such a way that its far-field behaviour can be accounted for, in the linear approximation, by the reemission of light by an oscillating dipole $\mathbf{p}$. The response of the island is estimated through its dipole strength, *i.e.* its effective polarizability tensor, which relates the dipole and the external field $\mathbf{p} = \overline{\alpha}\cdot\mathbf{E}_\mathrm{ext}$. By using the rotational symmetry along the z-axis, the $\overline{\alpha}$ tensor is diagonal with two main eigenvalues, one parallel $\alpha_\parallel$ and the other perpendicular α_z to the surface of the substrate. Of course, these polarizabilities depend on the charge induced in the

$$r_{\rm s} = \frac{n_1\cos\theta - n_2\cos\theta_{\rm t} + {\rm i}(\omega/c)\gamma}{n_1\cos\theta + n_2\cos\theta_{\rm t} - {\rm i}(\omega/c)\gamma} \tag{2.20a}$$

$$t_{\rm s} = \frac{2n_1\cos\theta}{n_1\cos\theta + n_2\cos\theta_{\rm t} - {\rm i}(\omega/c)\gamma} \tag{2.20b}$$

$$r_{\rm p} = \frac{(n_2\cos\theta - n_1\cos\theta_{\rm t})[1-(\omega/2c)^2\epsilon_1\gamma\beta\sin^2\theta] - {\rm i}(\omega/c)\gamma\cos\theta\cos\theta_{\rm t} + {\rm i}(\omega/c)n_1n_2\epsilon_1\beta\sin^2\theta}{(n_2\cos\theta + n_1\cos\theta_{\rm t})[1-(\omega/2c)^2\epsilon_1\gamma\beta\sin^2\theta] - {\rm i}(\omega/c)\gamma\cos\theta\cos\theta_{\rm t} - {\rm i}(\omega/c)n_1n_2\epsilon_1\beta\sin^2\theta} \tag{2.20c}$$

$$t_{\rm p} = \frac{2n_1\cos\theta[1+(\omega/2c)^2\epsilon_1\gamma\beta\sin^2\theta]}{(n_2\cos\theta + n_1\cos\theta_{\rm t})[1-(\omega/2c)^2\epsilon_1\gamma\beta\sin^2\theta] - {\rm i}(\omega/c)\gamma\cos\theta\cos\theta_{\rm t} - {\rm i}(\omega/c)n_1n_2\epsilon_1\beta\sin^2\theta} \tag{2.20d}$$

particle, on the geometry and on the frequency dependent dielectric constants.

Far away from the island centre $\mathcal{O}$, the spheroidal and spherical expansions become equivalent, *i.e.*

$$Z_\ell^m(\xi,a) \simeq (a\xi)^{-\ell-1} \simeq r^{-\ell-1}, \tag{2.13a}$$

$$Y_\ell^m(\arccos\eta,\phi) \simeq Y_\ell^m(\theta,\phi) \tag{2.13b}$$

for $\xi \to \infty$. Therefore, the polarizability tensor elements for an oblate or prolate island, normal or perpendicular to the surface of the substrate respectively, can simply be related to the multipolar coefficients A_{10} and A_{11} of the potential in medium 1:

$$\alpha_z(0) = \frac{2\pi\epsilon_1 A_{10}}{\sqrt{\pi/3}E_0\cos\theta_0}, \tag{2.14a}$$

$$\alpha_\parallel(0) = \frac{-4\pi\epsilon_1 A_{11}}{\sqrt{2\pi/3}E_0\sin\theta_0}. \tag{2.14b}$$

For the cap case, the direct multipoles are located at $\mathcal{O}'$, below the surface of the substrate. In equations (2.14), ϵ_1 must be replaced by ϵ_2. Furthermore, the external field, by which A_{10} and A_{11} are divided, is the transmitted incident field in medium 2, *i.e.*, the substitution $E_0\cos\theta_0 \to \epsilon_1/\epsilon_2 E_0\cos\theta_0$ has to be made. Hence, the equivalent formulae to equations (2.14) for the cap case becomes:

$$\alpha_z(0) = \frac{2\pi\epsilon_2 A_{10}}{(\epsilon_1/\epsilon_2)\sqrt{\pi/3}E_0\cos\theta_0}, \tag{2.15a}$$

$$\alpha_\parallel(0) = \frac{-4\pi\epsilon_2 A_{11}}{\sqrt{2\pi/3}E_0\sin\theta_0}. \tag{2.15b}$$

2.3.2 The Fresnel coefficients: reflection, transmission and absorption

For low island density, the island polarizabilities are simply related to the surface susceptibilities (Sect. 1):

$$\beta_{\rm e}(d) = \frac{\rho\alpha_z(0)}{\epsilon_1^2}, \tag{2.16a}$$

$$\gamma_{\rm e}(d) = \rho\alpha_\parallel(0). \tag{2.16b}$$

where ρ is the number of particles per unit surface area (particle density). In these equations, $z = d$ means that the choice of the dividing surface for susceptibilities is along the substrate plane. For a cap, the dipole is shifted from the point $\mathcal{O}$ to just below the surface and crosses this surface. It can be proved [7] that $\alpha_z(0) = \alpha_z(-d+0^+) = (\epsilon_2/\epsilon_1)^2\alpha_z(-d+0^-)$ and $\alpha_\parallel(0) = \alpha_\parallel(-d+0^+) = \alpha_\parallel(-d+0^-)$, which leads to the following expressions of the surface susceptibilities:

$$\beta_{\rm e}(-d) = \frac{\rho\alpha_z(0)}{\epsilon_2^2}, \tag{2.17a}$$

$$\gamma_{\rm e}(-d) = \rho\alpha_\parallel(0). \tag{2.17b}$$

Dimensionless susceptibilities quantities can be introduced:

$$\hat\beta = \frac{\beta_{\rm e}(\pm d)}{\rho V} \sim \hat\alpha_z, \qquad \hat\gamma = \frac{\gamma_{\rm e}(\pm d)}{\rho V} \sim \hat\alpha_\parallel \tag{2.18}$$

where $\hat\alpha_z = \alpha_z/V$ and the same for $\hat\alpha_\parallel$. V denotes the volume of the particle located above the substrate:

$$V({\rm oblate}) = \frac{1}{3}\pi a^3\xi_0(1+\xi_0^2)(2 \pm t_{\rm r} \mp t_{\rm r}^3), \tag{2.19a}$$

$$V({\rm prolate}) = \frac{1}{3}\pi a^3\xi_0(\xi_0^2-1)(2 \pm t_{\rm r} \mp t_{\rm r}^3). \tag{2.19b}$$

In the previous equations, the (+) sign should be used for an island and (−) for a cap. Bearing in mind that the polarisability is directly proportional to V of the particle, these reduced susceptibilities do not depend on it. The dependence on other parameters, such as those characterizing the shape of the particle, can hence be described more easily. The quadrupole susceptibilities τ and δ, which include the non-local response of the surface quadratic in d/λ, are ignored herein since absorption dominates in the metallic particles under consideration. However, for the case of dielectric particles, these terms should be included [7].

The susceptibilities γ and β modify the boundary conditions in such a way that the amplitudes of the reflected and transmitted in $s-$ or p-polarisation states can be expressed as [8]:

See equations (2.20a, 2.20b, 2.20c, 2.20d) above

where $n_1 = \sqrt{\epsilon_1}$ and $n_2 = \sqrt{\epsilon_2}$ are the refractive indexes of the ambient medium and substrate, respectively, θ the angle of incidence and $\theta_{\rm t}$ the angle of the transmitted beam given by Descartes law. The reflectance and transmittance

are obviously given by the flux conservation of Poynting vector:

$$R_{\rm s} = |r_{\rm s}|^2, \qquad R_{\rm p} = |r_{\rm p}|^2, \qquad (2.21a)$$

$$T_{\rm s} = |t_{\rm p}|^2 \frac{n_2 \cos\theta_{\rm t}}{n_1 \cos\theta}, \qquad T_{\rm p} = |t_{\rm p}|^2 \frac{n_2 \cos\theta_{\rm t}}{n_1 \cos\theta}. \qquad (2.21b)$$

Here n_1 and n_2 are supposed to be real for insuring the physical existence of the transmitted field in the substrate.

2.4 The influence of the particle shape on the optical absorption

In this section, the importance of the aspect ratio in modelling the optical response of particles is illustrated by performing a numerical implementation of the model in the case of silver on alumina. To numerically compute the multipolar expansion coefficients, the set of linear equations (2.12) has to be truncated at some order M. Most often, the calculations are only aimed at determining the polarizability of the particles *via* the estimates of the terms A_{10} and A_{11} of the multipolar expansion of the interaction of the particle with the substrate. In practice, M is increased until these parameters do not evolve any longer. However, a more stringent test of the convergence consists in examining the fulfillment of the boundaries conditions on the surface of the particle [15]. In most cases, $M = 16$ is high enough to achieve a reasonable convergence of the numerical calculations. Two drawbacks are encountered in calculations. When $t_{\rm r}$ is close to unity, a divergence is brought about by cancellations of big numbers which leads to round-off errors. Moreover, a particle close to a truncated sphere is not well described in spheroidal coordinates. Indeed, the calculation for a sphere, which corresponds to the limits $\xi_0 \to \infty$ and $a \to 0$ with $\xi_0 a = R$, is untractable in the spheroidal model since it requires the computation of very large numbers. In this limit, the supported particles have been represented by means of the previously described model of truncated spheres [16,17].

A numerical implementation of the above model is performed in the case of silver on Al_2O_3. The dielectric constants are extracted from the compilation of Palik [21]. The silver clusters, around 10 nm in diameter, are much smaller than optical wavelengths ($\lambda \sim 10^2$ nm). Hence a finite-size correction has been applied to the dielectric constant of silver. The reduction of the mean-free path of the s-conduction electrons with respect to the bulk, results in a shorter relaxation time τ. The classical expression for the dielectric function is [1,22]:

$$\epsilon(\omega) = \epsilon_{\rm B}(\omega) + \frac{\omega_{\rm p}^2}{\omega^2 + {\rm i}\omega\tau_{\rm B}^{-1}} - \frac{\omega_{\rm p}^2}{\omega^2 + {\rm i}\omega\tau^{-1}} \qquad (2.22)$$

where $\epsilon_{\rm B}$ is the bulk dielectric function, $\hbar\omega_{\rm p}$ is the plasma frequency of s-electrons alone, and $\hbar/\tau_{\rm B}$ is the bulk relaxation time. By taking $\lambda_{\rm B} = 43$ nm, $\hbar\omega_{\rm p} = 9.17$ eV, $\hbar/\tau_{\rm B} = 0.018$ eV, $\hbar v_{\rm F} = 0.91$ eV nm and $\hbar/\tau = \hbar/\tau_{\rm B} + \hbar v_{\rm F}/R = 0.2$ eV, the corrected dielectric function of silver has been plotted in Figure 3 for the UV-visible range.

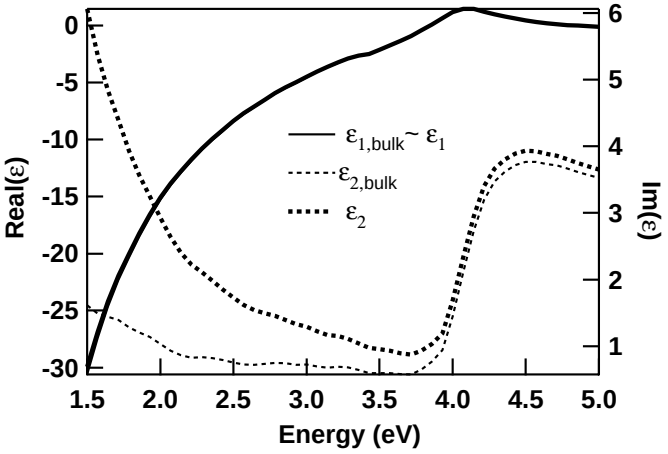

Fig. 3. The dielectric constant of silver: bulk values from E.D. Palik (thin lines) and corrected ones with a reduced relaxation time $\hbar/\tau = 0.2$ eV (bold lines).

Figure 3 clearly demonstrates that finite-size corrections are worth considering, since the imaginary part of the dielectric function of the particle is significantly increased with respect to the bulk values. These corrected values for the dielectric function of silver will be used in all numerical calculations presented below. The matrix elements contained in equations (2.12) were calculated as described in Appendix C.

As compared to the truncated spherical model [15–17] or that of supported spheroids [23], the present model has the capability of dealing with a great variety of particle shapes, ranging from flat discs to needles. To highlight the influence of the particle shape on the optical response, the real and imaginary components of the reduced susceptibilities $\hat{\beta} \sim \hat{\alpha}_z$ and $\hat{\gamma} \sim \hat{\alpha}_{\parallel}$ are plotted in Figure 4 as functions of $x = 1/(1 + a_{\rm r})$, for a fixed truncation ratio $t_{\rm r} = 0$, which corresponds to a hemispheroidal shape. The energy of the light was chosen to be $E = 2.5$ eV ($\epsilon_2 = 3.15$ and $\epsilon_3 = -8.364 + {\rm i}1.729$). Indeed, the strong peaks in the imaginary parts of the reduced susceptibilities $\hat{\beta}$ and $\hat{\gamma}$, which appear at $a_{\rm r} = 0.25$ (Fig. 4a) and $a_{\rm r} = 1.5$ (Fig. 4b), respectively, are directly related to maxima in the absorption of the light [24]. This demonstrates that the absorption by particles smaller than the wavelength are highly sensitive to their shape. To the first order, the maxima are associated with "dipolar" modes excited in the particle. Such modes can be visualized by mapping the potential around the particle (Fig. 5) for incident fields E_0 either parallel ($\theta_0 = \pi/2$) or normal ($\theta_0 = 0$) to the surface. The equipotential lines of the potentials in units of $E_0 R_\perp$ are pinned around the triple contact line for $a_{\rm r} = 1.5$ whereas a less intense dipolar vibration is seen in the normal direction for $a_{\rm r} = 0.25$. It is worth noting that Figures 5a and c present a mirror plane perpendicular to the figure (azimuthal function $m = 1$) whereas Figures 5b and d present a revolution axis along z for $\theta = 0$ ($m = 0$).

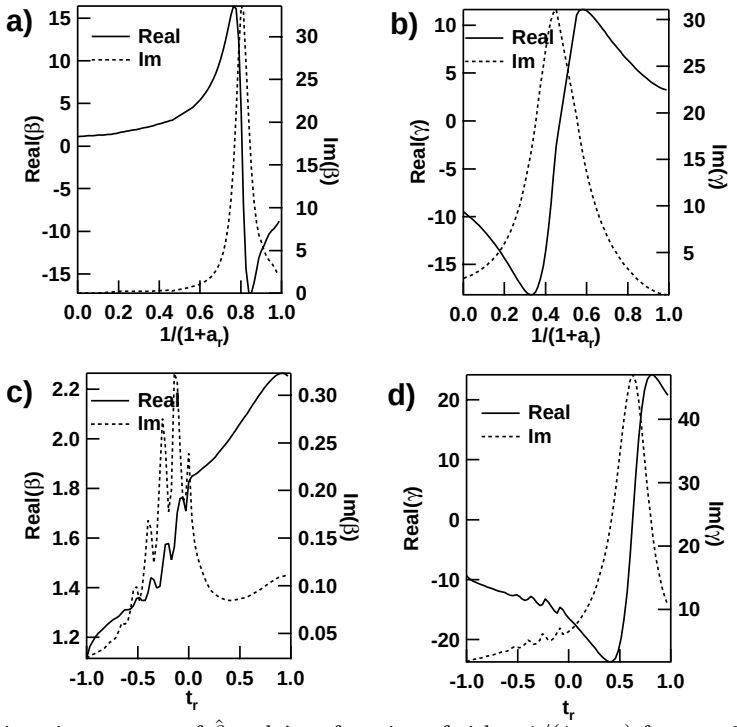

Fig. 4. Plots of the real and imaginary parts of $\hat{\beta}$ and $\hat{\gamma}$ as function of either $1/(1+a_{\rm r})$ for $t_{\rm r}=0$ (Figs. 4a–b) or $t_{\rm r}$ for $a_{\rm r}=3$ (Figs. 4c–d). The values for the dielectric constants are $\epsilon_1=1$, $\epsilon_2=3.15$, $\epsilon_3=(-8.364, 1.729)$. The multipolar order was fixed at $M=16$ in the framework of the truncated spheroid model. These curves correspond to dotted lines in Figure 6.

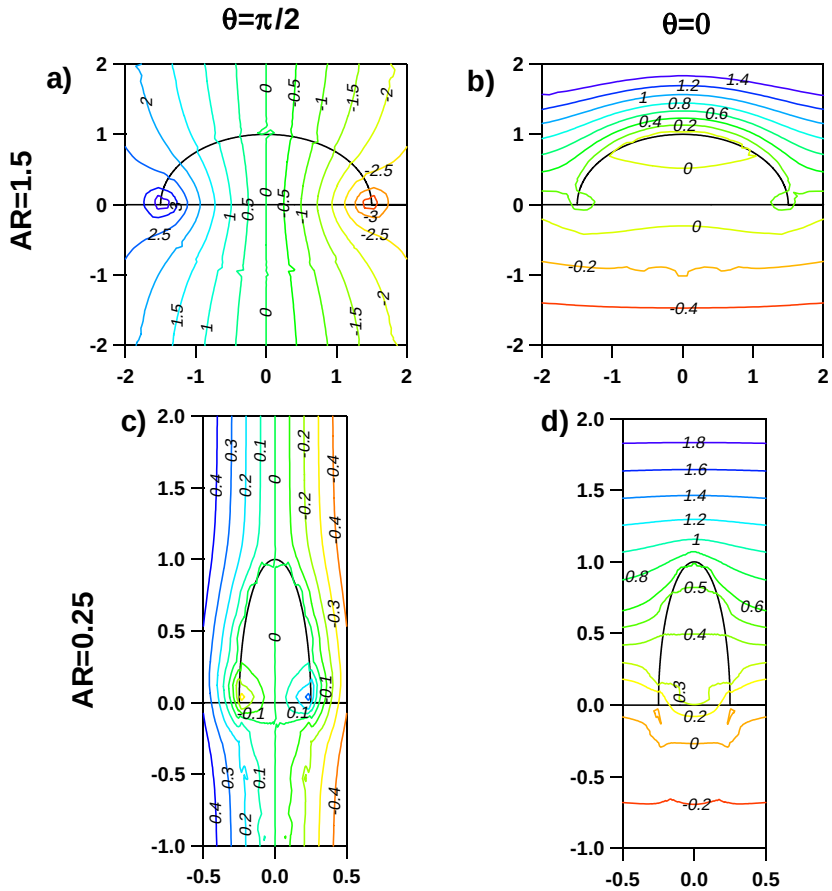

Fig. 5. The equipotential lines at the same fixed energy as in Figure 4 for the resonance aspect ratio for $t_{\rm r}=0$ (Figs. 4a–b): $a_{\rm r}=1.5$ and $a_{\rm r}=0.25$. Two directions of excitation for the incident field E_0 are used: $\theta=0$ or $\theta=\pi/2$. The values of the potentials are given in units of $E_0 R_\perp$ while the 1st and 2nd axis are in dimensionless units: $x/R_\parallel$ and $y/R_\perp$.

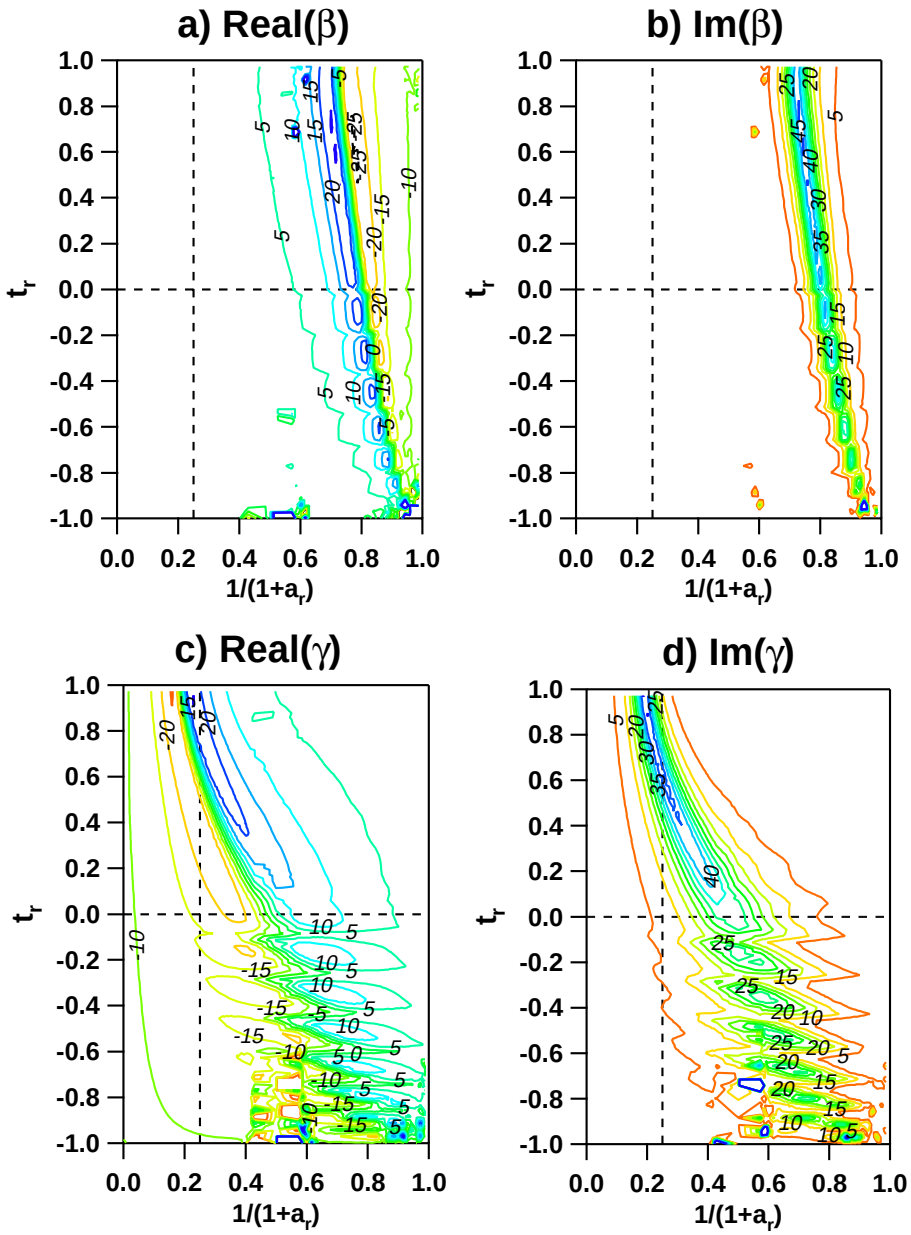

Fig. 6. The isovalues of the real and imaginary parts of $\hat{\beta}$ and $\hat{\gamma}$ in a $(1/(1+a_{\rm r})$-$t_{\rm r})$ plane. The energy is fixed at $E = 2.5$ eV and the dielectric constants are the same used in Figures 4. The multipolar order in the interaction of this particle with the substrate was again fixed at $M = 16$ in the framework of the truncated spheroid model. The dotted lines correspond to the cuts of Figures 4.

In Figure 6, the isovalues of the real and imaginary parts of the the reduced quantities $\hat{\beta}$ and $\hat{\gamma}$, which have been determined at multipolar order $M = 16$, are plotted in the $(x, t_{\rm r})$-plane. Resonances in a prolate (oblate) particle manifest themselves upon normal (parallel) excitations. Interestingly, their locations are mainly determined by the aspect ratio $s_{\rm r}$ of the particle since the most intense contour lines for the imaginary part of $\hat{\beta}$ and $\hat{\gamma}$ closely follow a constant aspect ratio line $s_{\rm r}$ as seen from Figure 2 ($s_{\rm r} \simeq 0.75$ for $\hat{\beta}$ and $s_{\rm r} \simeq 3.5$ for $\hat{\gamma}$). Less intense well localized absorptions are seen for $\mathrm{Im}(\hat{\beta})$ or $\mathrm{Im}(\hat{\gamma})$ for a cap particle ($t_{\rm r} < 0$). A cut along the line $a_{\rm r} = 3$ (vertical dashed line) is presented in Figures 4c–d. Despite the difference in magnitude of the polarizability parallel and normal to the surface, numerous small absorptions features seen in $\mathrm{Im}(\hat{\beta})$ are attributed to multipolar absorptions and such modes [25,26] will be the main topic of a forthcoming paper.

Several models can be used to interpret light absorption by supported particles, namely the effective dielectric medium and the dipolar theories. The former clearly does not include neither the electromagnetic coupling with the substrate nor the anisotropy of the optical response of the particles [1]. By accounting for interactions with the

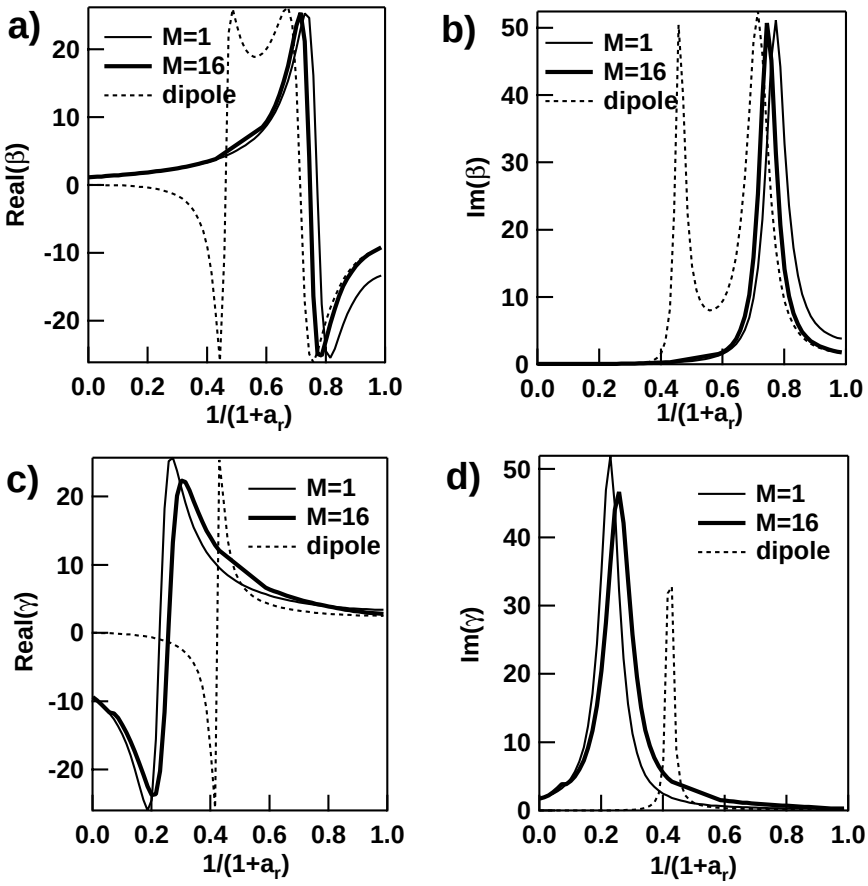

Fig. 7. The comparison for $\hat{\beta}$ and $\hat{\gamma}$ between the Yamaguchi dipole model (dotted line) and the $M = 1$ (thin line), $M = 16$ (bold line) approximations of the present model. The truncation parameter $t_{\rm r}$ is set equal to 0.6 as the distance between the dipole and the surface in the Yamaguchi theory $d = 0.6R_{\perp}$. The values used for ϵ_i are the same as those used in Figure 6.

substrate up to dipolar order, the polarizabilities α are given by:

$$\alpha_{\parallel}(d) = \frac{\alpha_{\parallel}}{1 + A\alpha_{\parallel}}, \qquad \alpha_z(d) = \frac{\alpha_z}{1 + 2A\alpha_z} \tag{2.23}$$

where $\alpha_{\parallel}$ and α_z are the free particle polarizabilities and d is the distance from the dipole to the surface of the substrate. The dipole image is introduced through $A = (32\pi\epsilon_1 d^3)^{-1} (\epsilon_1 - \epsilon_2) / (\epsilon_1 + \epsilon_2)$. This approach describes the main physics of the depolarization process, but neglects all the higher order multipoles as well as the real shapes of the objects.

To show the influence of these higher order multipoles, the reduced polarizabilities $\hat{\beta}$ and $\hat{\gamma}$ have been plotted in Figures 7 as a function of $1/(1 + a_{\rm r})$ for the model of Yamaguchi *et al.*, equation (2.23) and within the $M = 1$ and $M = 16$ approximations of the present model. The truncation ratio used to obtain the results of Figures 7 was $t_{\rm r} = 0.6$. Calculations at order $M = 1$ (dipolar order) and $M = 16$ do not differ very much. In fact, the model spectrum does not evolve anymore for $M > 16$. This is the reason why this value has been chosen for all calculations in the present work. However, the discrepancy between dipolar model [5,6] and the spheroidal model is significant. This in particular is true for the parallel polarizability $\hat{\gamma}$ (Figs. 7c–d). Indeed, the dipolar model overestimates the interaction with the substrate [23] and underestimates the axial ratio corresponding to the resonance. Moreover, the damping, *i.e.* the resonance width, is drastically too small for this type of model. In the case of $\hat{\beta}$, the axial ratio of the resonance is ill-defined giving rise to a double peak (Figs. 7a and b) although the amplitudes seem to be correctly described. This phenomenon is due to the strange behaviour of the depolarization factors in the dipolar model for oblate particles [23]. Thus, the correct description of both the shape of the particle and the particle-substrate interaction is a key ingredient of a quantitative approach to the light absorption by supported metallic particles. In particular, fitting the extinction positions with the axial ratio and the position of the dipole d [27] leads obviously to erroneous conclusions.

Another way to probe the islands excitations which is more appealing from an experimental point of view is to vary the wavelength or energy, E, of the incident light. In Figures 8, the case of a hemispheroid ($t_{\rm r} = 0$) of silver on Al_2O_3 with $\hbar/\tau = 0.2$ eV is considered in the $(E,1/(1 + a_{\rm r}))$ plane. Silver is a peculiar metal since it has a strong plasmon oscillation which is poorly damped

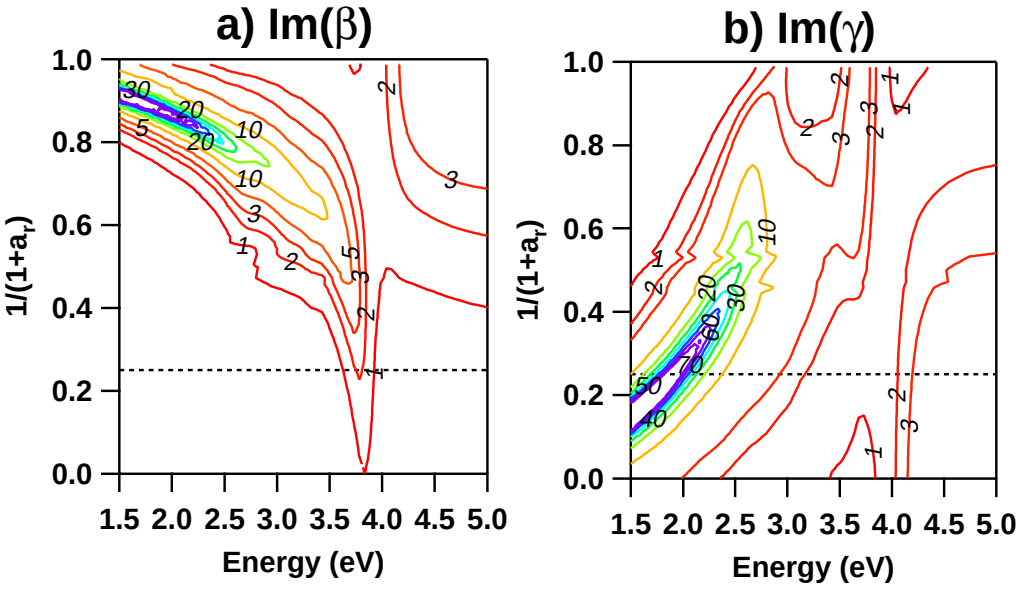

Fig. 8. Isolines values for $\hat{\gamma}$ and $\hat{\beta}$ in the (energy,$1/(1+a_{\rm r})$) plane. The truncation parameter and the number of multipoles are $t_{\rm r}=0$ and $M=16$ respectively. The dielectric constant are that of Al_2O_3 for the substrate and that of silver for the cluster. The optical behaviour for silver is corrected from finite-size effects by using a relaxation time $1/\tau=0.2$ eV.

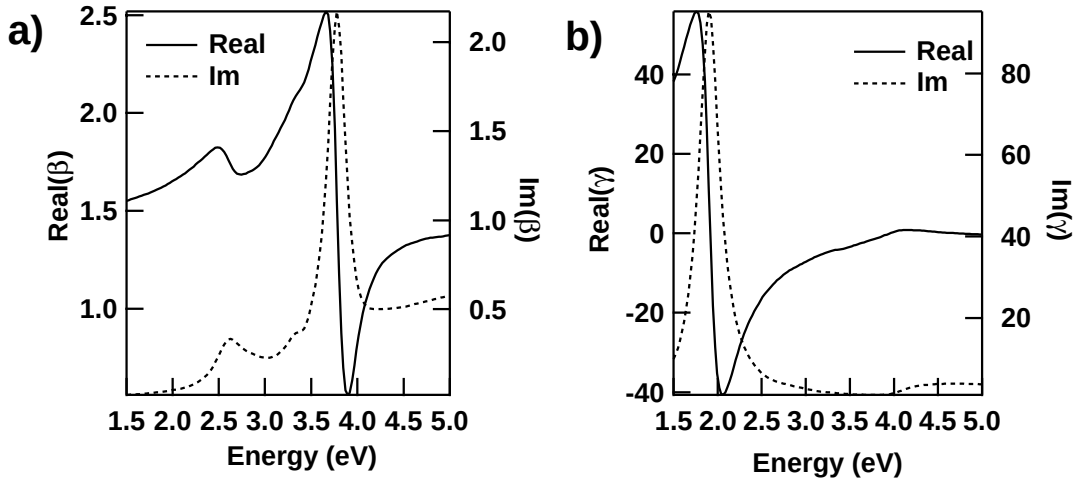

Fig. 9. Evolution of $\hat{\beta}$ and $\hat{\gamma}$ with energy for parameters $M=16$, $t_{\rm r}=0$, and $a_{\rm r}=3$. This value for $a_{\rm r}$ corresponds to the dashed line indicated in Figures 8. The dielectric constants are the same used in Figure 6.

by interbands transition contrary to transition metals. Its dielectric constant is such that upon either flattening or interaction with the substrate, the splitting of the Mie resonance of the sphere falls in the UV-visible spectral range. This is clearly seen in Figure 8 where for every axial ratio $a_{\rm r}$ two absorption resonances of different intensities located at different energies are excited. For instance, for an oblate particle of $a_{\rm r}=3$ indicated by a dashed line in Figure 8, a weak resonance associated with the dipole excitation perpendicular to the surface is seen in $\hat{\beta}$ at an energy around $E=3.7$ eV (Fig. 9a), while a strongest absorption resonance is along the surface at around $E=2$ eV (Fig. 9b).

3 Application to metal particles supported on oxide substrates

In this section, the relevance of the above model is highlighted by several examples. Previous experimental data concerning silver deposit on MgO [2,15] are then revisited in the light of the present approach to more finely characterize the shape of the supported clusters. Finally the model is also used in the cases of both aluminium and titanium thin films to show that it can be applied to various metals.

3.1 Aspect ratio of silver particles on a magnesium oxide substrate

The principle of the experiments presented herein consists in examining metallic thin films by Surface Differential Reflectance (SDR) in an ultra-high vacuum chamber. The relative reflectivity of the sample defined as:

$$\frac{\Delta R}{R}(\omega) = \frac{R(\omega) - R_0(\omega)}{R_0(\omega)}, \tag{3.1}$$

where $R_0(\omega)$ is the bare substrate (Fresnel) reflectivity, is measured, in real time and *in situ* during the metal deposition. Here, the incident light was UV-visible light provided by a deuterium lamp. It was p-polarized and the angle of incidence was 45°. The scattered light was analyzed by a grating spectrometer *via* an optical fiber. Spectra were recorded on a 1024 silicon diode array connected to a computer.

The vacuum chamber was equipped with a X-ray Photoemission Spectrometer (XPS) and a Low Energy Electron Diffraction (LEED) Princeton Res. Instr. MgO(100) samples were cleaved from crystals provided by Canadian Substrates in a glove bag filled with dry nitrogen and directly connected to the load-lock system of the vacuum chamber, so that these samples could be introduced in vacuum without any contact with the ambiant air. The α-$Al_2O_3(0001)$ crystals were polished samples provided by Mateck. Samples were cleaned by an already described method [28]. The cleanliness of the surfaces was checked by XPS and good LEED patterns were recorded on each type of crystal. Silver was deposited from an alumina cell and aluminium from a boron nitride cell. In the case of aluminium, the cell was degassed for days in vacuum, at a temperature just above the melting temperature of aluminium (933 K). Prior to being used for thin film deposition, it was annealed at 1273 K for a few hours. Titanium was evaporated from a titanium filament wrapped round a tungsten wire. The system was carefully outgassed. All sources were checked to provide pure metal fluxes, in particular in the cases of aluminium and titanium. Aluminium and silver fluxes have been calibrated by means of a quartz balance. Titanium coverages were determined by XPS analysis of the titanium-covered substrates. For Ag/MgO, *ex situ* techniques [2] have allowed for the determination of the mean cluster density $\rho = 1.9 \pm 0.5\,10^{11}$ cm^{-2} and the particle radius as seen from above $R = 8.2 \pm 1.5$ nm (Tab. 1). The experimental spectrum (open circles in Fig. 10), is dominated by two features which are associated with the excitation of Mie resonances by the p-polarized incident light.

Up to now, the assumption has been made that the particles are non-interacting. In fact in the quasi-static limit the polarizabilities must be renormalized by accounting for a dipolar interaction of a given particle with the surrounding particles and their images [7,11,17,29]. For the island case, such renormalized polarizabilities are given by [7,11,17,29]:

Table 1. Comparison between experimental and theoretical parameters values for the sphere and spheroid model. (f) corresponds to parameters whose value has been fixed to the experimental value.

Model	$R_\parallel$(nm)	$R_\perp$(nm)	t_r	ρ(cm^{-2})	s_r	χ^2
spheroid	8.2(f)	4.8	0.27	$1.9\,10^{11}$(f)	2.7	0.18
sphere 1	8.2(f)	8.2(f)	0	$1.9\,10^{11}$(f)	2	0.30
sphere 2	6.8	6.8	0.11	$2.6\,10^{11}$	1.8	0.25

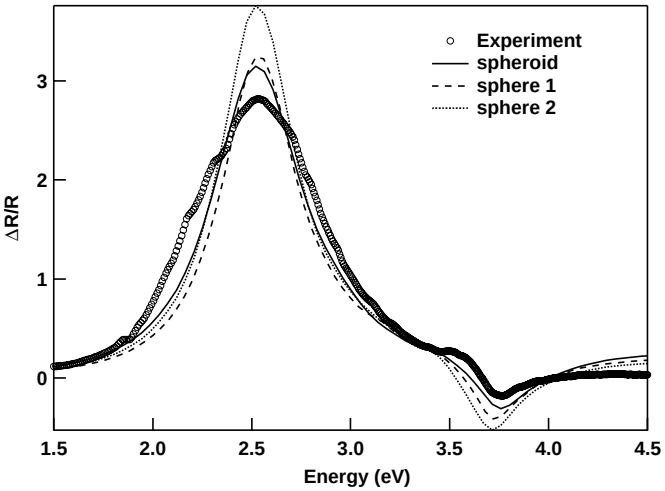

Fig. 10. Theoretical and experimental (points) differential reflectivity spectra for Ag/MgO(100). Comparison of the spherical (dotted lines) and spheroidal model (continuous line) at order $M = 16$ (see text for the parameter).

$$\alpha_z(0) = \bar{\alpha}_z \left\{ 1 - \frac{\bar{\alpha}_z}{2\pi\epsilon_1 L^3} \left[S_{20} - \left(\frac{\epsilon_1 - \epsilon_2}{\epsilon_1 + \epsilon_2} \right) \tilde{S}^{\mathrm{r}}_{20} \right] \sqrt{\frac{4\pi}{5}} \right\}^{-1}, \tag{3.2a}$$

$$\alpha_\parallel(0) = \bar{\alpha}_\parallel \left\{ 1 + \frac{\bar{\alpha}_\parallel}{4\pi\epsilon_1 L^3} \left[S_{20} + \left(\frac{\epsilon_1 - \epsilon_2}{\epsilon_1 + \epsilon_2} \right) \widetilde{S}^{\mathrm{r}}_{20} \right] \sqrt{\frac{4\pi}{5}} \right\}^{-1} \tag{3.2b}$$

and for the cap particle, ϵ_1 and ϵ_2 have to be interchanged. Here $\bar{\alpha}_z$ and $\bar{\alpha}_\parallel$ denote the polarizabilities of a single cluster interacting with the substrate as calculated from equations (2.14) and (2.15). The functions S_{20} and $\tilde{S}^{\mathrm{r}}_{20}$ are defined by [7]:

$$S_{20} = \sum_{i \neq 0} \left(\frac{L}{r} \right)^3 Y_2^0(\theta, \phi)|_{\mathbf{r}=\mathbf{R_i}}, \tag{3.3a}$$

$$\widetilde{S}^{r}_{20} = \sum_{i \neq 0} \left(\frac{L}{r} \right)^3 Y_2^0(\theta, \phi)|_{\mathbf{r}=\mathbf{R_i^r}}, \tag{3.3b}$$

where L is the lattice constant. The lattice sums S_{20} and $\widetilde{S}^{\mathrm{r}}_{20}$ defined in equations (3.3) describe the dipole-dipole interaction of a dipole with the surrounding dipoles and images placed at $\mathbf{r} = \mathbf{R_i}$ and $\mathbf{r} = \mathbf{R_i^r}$ respectively. Notice

the difference between this approach, where the limit $i = 0$ is excluded from the lattice sums of equations (3.3) and instead included in $\bar{\alpha}$, and the dipolar model [5,6] (*cf.* Eqs. (2.23)). The dipole approximation [30] was shown to be sufficient to model particle-particle interactions up to rather high coverage (50%) for spheres. Moreover, a calculation up to quadrupolar order for truncated sphere has demonstrated that the difference with dipolar order was negligible [31] at this experimental coverage. After renormalizing the polarizabilities in agreement with equations (3.2), the susceptibilities β and γ are calculated by means of equations (2.16) and (2.17) and the reflectivity from equations (2.20) and (2.21).

In the computational process of model SDR-spectra (for $M = 16$), both the density ρ and the apparent island radius, $R_{\parallel}^{\mathrm{app}}$, parallel to the substrate were kept constant at the experimental values (Tab. 1). The type of array (square, hexagonal or random) being unimportant at this coverage [30,31], a square array of clusters was used. A finite size correction in the dielectric constant was applied:

$$\frac{1}{\tau} = \frac{1}{\tau_{\mathrm{B}}} + \frac{v_{\mathrm{F}}}{R'} \tag{3.4}$$

with R' being half of the smallest dimension of the physical particle (medium 3). A χ^2-factor defined by:

$$\chi^2 = \frac{1}{N}\sum_{i=1}^{N}\left[\left(\frac{\Delta R}{R}\right)_{\mathrm{the}}(E_i) - \left(\frac{\Delta R}{R}\right)_{\mathrm{exp}}(E_i)\right]^2 \tag{3.5}$$

was used to determine the best theoretical parameters that fit the experimental DRS-spectrum. The comparison between the experimental spectrum (open circles) and the fits with spherical and spheroidal models are shown in Figure 10. In the spherical model 1, all parameters are allowed to vary [15]. The spherical model 2 as well as the spheroidal model consist in finding the best truncation at fixed density ρ and apparent radius R_{app}. The best χ^2-factor with the experimental parameters is achieved with the spheroidal model corresponding to the parameters $R_{\perp} = 4.8$ nm and $t_{\mathrm{r}} = 0.27$ ($s_{\mathrm{r}} = 2.7$) where the remaining fixed parameters are defined in Table 1. The truncated spheroidal model clearly brings about a new degree of freedom ($R_{\perp}$) in fitting the model to the experimental spectra. In this particular case, it allows to explore aspect ratios $s_{\mathrm{r}} > 2$ which can hardly be analyzed by means of the spherical model [15].

3.2 Aspect ratio of aluminium and titanium particles on an alumina substrate

Silver particles are a test bed for optical measurements. In this metal, the plasma energy is much reduced with respect to the free-electron prediction $\omega_{\mathrm{p}} = 9.2$ eV by the presence of a full d-band at 4–6 eV below the top of the hybridized s-p valence band. It amounts to $\omega_{\mathrm{p}}^{*} = \omega_{\mathrm{p}}/\sqrt{\mathrm{Re}(\epsilon_d)} = 3.8$ eV, where $\mathrm{Re}(\epsilon_d)$ is the real part of the contribution of the d band to the dielectric function of silver. Therefore, because the interactions with surrounding media tend to red-shift the plasma resonances below that value, the Mie absorption lines of silver mostly show up well inside the UV-visible range, which is the most accessible with the laboratory means. In addition, due to the fact that the interband sp-d transition threshold lies high enough (3.88 eV) to moderately damp the plasma oscillations, these resonances are sharp and intense. However, the above model can also be used in the case of (i) metals having resonances at energies much higher than those of silver and (ii) metals in which interband transitions broaden the resonances, as it is shown below in the case of aluminium and titanium depositions on alumina substrates.

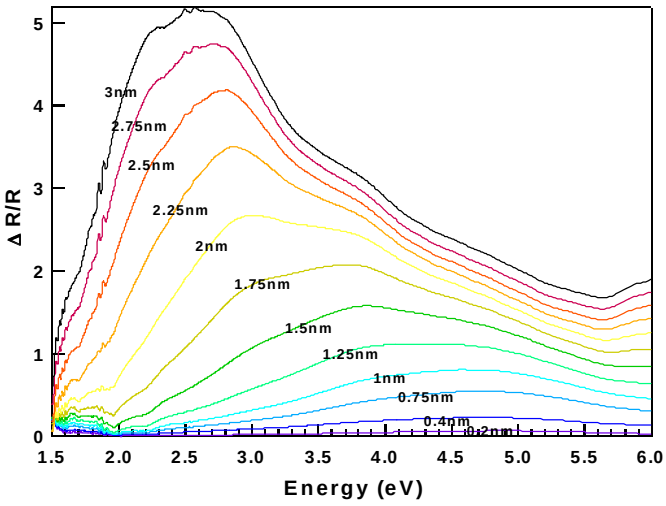

Fig. 11. SDR spectra collected during the deposition of aluminium on α-$Al_2O_3(0001)$ at 625 K. The average thickness is shown on each spectrum.

Aluminium behaves mostly as a Drude metal, with a Mie resonance expected at 9 eV and 6 eV for a sphere in vacuum or supported on an alumina substrate, respectively. SDR spectra recorded during the deposition of aluminium on α-$Al_2O_3(0001)$ held at 625 K are shown in Figure 11. A feature appears around 5 eV for an average thickness of 0.2 nm. It then shifts progressively towards lower energies. The absence of signal at the very beginning of the deposition is associated with the fact that, at that stage, the aluminium is not in a metallic form, a question that will be studied in more details in a forthcoming paper. Qualitatively, the observation of a Mie absorption band in the spectral range of the deuterium lamp, *i.e.* well below the resonance energy of a supported sphere (6 eV), indicates that aluminium clusters have high aspect ratios. Nevertheless, the existence of a band in the SDR spectrum discard the formation of a continuous layer which would instead result in a continuous increase in the reflected intensity toward the infrared region. In the same way, even at low coverages, the appearance of a resonance for an average thickness of aluminium

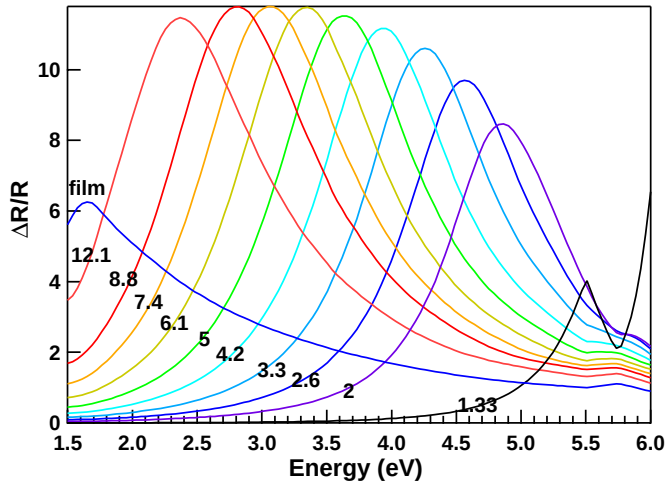

Fig. 12. Model SDR spectra calculated for aluminium clusters on alumina for different values of the aspect ratio which appear in figure. Clusters, which are modelled by hemispheroids ($t_r = 0$ and $M = 16$) forms an hexagonal array whose parameter is 20 nm. The average thickness of aluminium is 2 nm. Also shown is the spectrum corresponding to a continuous thin film.

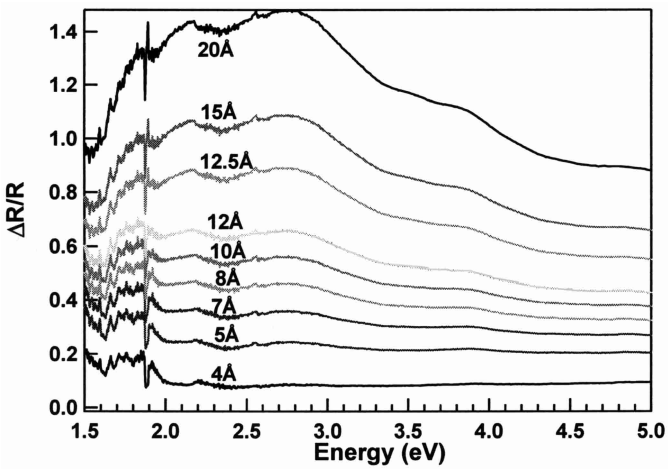

Fig. 13. SDR spectra collected during the deposition of titanium on α-$Al_2O_3(0001)$ at 300 K. The average thickness is shown on each spectrum.

of 0.2 nm is indicative of the formation of clusters (in order to form a dipole when excited by the electromagnetic field of the light [32]). This again corresponds to a three-dimensional (3D) growth mode. To put this in a more quantitative form, model spectra were calculated with the above formalism for hemispheroidal clusters of various aspect ratios, for an average thickness of 2 nm of aluminium (Fig. 12). By comparing model and experiment, it appears that the value of the aspect ratio which best fits the experiment is close to 8. Therefore, the suggestion that aluminium deposited on alumina forms flat-top 3D clusters is fully supported by the model spectra. It is worth mentioning that experimental spectra are much broader than model spectra. This might obviously arise from some scattering in the aspect ratios of the supported aluminium clusters. However, experimental lines also show very visible extra features which are reminiscent of those which show up when the size of the clusters becomes not negligible with respect to the wavelength of the incident light or, in other words, when the optical response no longer obey the quasi-static limit [1].

SDR spectra collected during the deposition of titanium on α-$Al_2O_3(0001)$ at 300 K are shown in Figure 13. Titanium being an early transition metal, its plasma resonance is strongly damped by interband transitions, in particular around 2 eV and 4 eV [33]. Consequently, the resulting reflectivity spectra show broad features peaking slightly below 3 eV (Fig. 13). As in the case of aluminium deposition, the absence of optical response up to 0.4–0.5 nm is associated with the oxidation of the very first layer of titanium deposited on the alumina substrate [34]. Calculated spectra have been derived from both the truncated sphere model [15] and the above-mentioned truncated spheroidal model, for aspect ratios up to two and higher than two, respectively (Fig. 14). The experimental spectra clearly differ from models obtained by assuming a two-dimensional growth which should correspond to the case of a perfect wetting. Instead, the models which best agree with experiment are those which are derived for aspect ratio values ranging between 4 and 8. These observations meet the high energy electron diffraction results of Dehm *et al.* [35], and Suzuki *et al.* [36]. The diffraction patterns recorded by these authors show lines which indicate a trend toward two-dimensional growth mode.

Both aluminium and titanium films deposited on α-$Al_2O_3(0001)$ substrates behave in a quite similar manner. They both grow in a Volmer-Weber mode. However, although they form 3D clusters, these cluster show very high aspect ratios. This is consistent with experiments by atomic force microscopy on α-$Al_2O_3(0001)$ which evidenced large flat-top clusters and a rather uniform coverage for aluminium and titanium depositions, respectively, attributing in particular these growth modes to a chemical interaction at the metal/alumina interface [34].

4 Conclusion

An approach to evaluate the optical properties of supported particles in the quasi-static limit has been introduced by modelling particles with truncated spheroids. The island polarizabilities are evaluated by a multipolar expansion of the potential in spheroidal coordinates. This particle shape offers the opportunity to describe a much wider range of island morphologies than the previously published models of truncated spheres or supported spheroids. In addition, the computational limit for the description of the aspect ratio of particles by the truncated sphere model is by-passed by the truncated spheroid model.

By using the present approach, the aspect ratio is demonstrated to tremendously influence the optical response of particles. Growths of Ag/MgO(100),

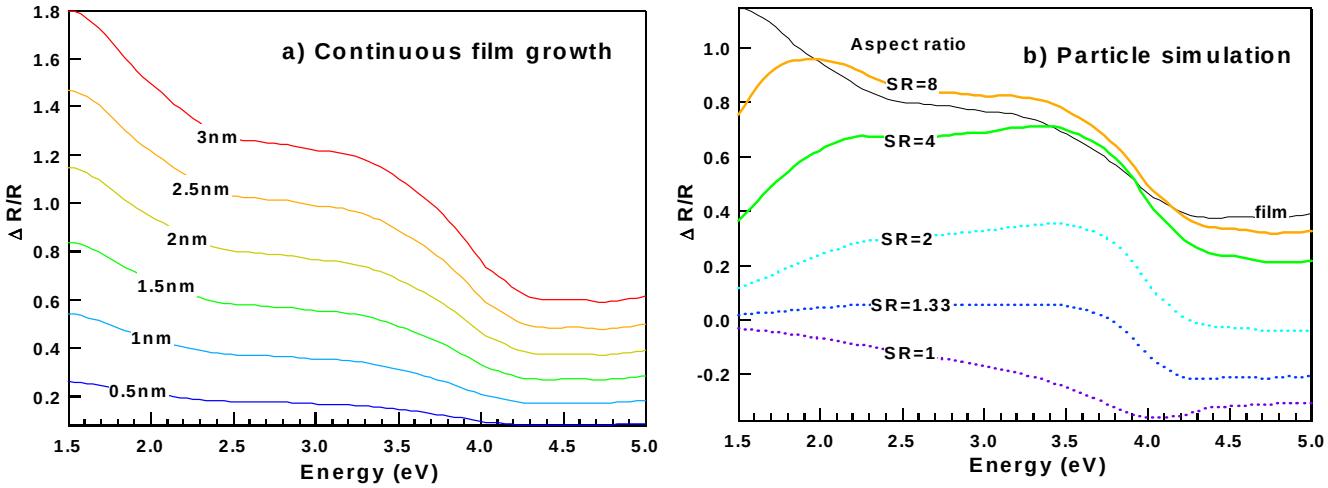

Fig. 14. Model SDR spectra calculated for titanium deposited on alumina: (a) layer by layer thin film with different thicknesses (shown in the figure); (b) titanium clusters on a hexagonal array (same parameters as in the case of aluminium), the average thickness being 2 nm; the truncated sphere model (dotted line) is used for aspect ratios lower than two and the truncated spheroid model (continuous line) for aspect ratios higher than two; the optical response of the continuous thin film is also given.

$Al/Al_2O_3(0001)$ and $Ti/Al_2O_3(0001)$ thin films are examined by Surface Differential Reflectance (SDR) and model spectra are calculated. Although three-dimensional growth mode are observed for all systems, aluminium and titanium deposited on alumina are shown to form particles with very high aspect ratios. These cases illustrate the capability of the present model to deal with the optical response of particles of various metals with different shapes.

Appendix A: The spheroidal coordinate system

The definition of the spheroidal coordinate system (ξ, η, ϕ) is different for a prolate and an oblate spheroid [19]. In the case of an oblate spheroid (Fig. 1), the long (l) and short (s) axis parallel and normal to the surface of the substrate are $R_\mathrm{l} = 2a\sqrt{\xi_0^2+1}$ and $R_\mathrm{s} = 2a\xi_0$, respectively. Furthermore, the quantity a denotes the radius of the ring of foci and $\xi = \xi_0$ defines the surface of the spheroid. Cartesian coordinates are related to spheroidal coordinates by [19]:

$$\xi = \left[\left(\frac{\rho_1+\rho_2}{2a}\right)^2 - 1\right]^{1/2}, \quad \eta = \pm\left[1-\left(\frac{\rho_1-\rho_2}{2a}\right)^2\right]^{1/2}, \quad \phi = \arctan\left(\frac{y}{x}\right) \tag{A1}$$

with

$$\rho_1 = [z^2 + (x + a\ \cos\ \phi)^2 + (y + a\ \sin\ \phi)^2]^{1/2},$$
$$\rho_2 = [z^2 + (x - a\cos\phi)^2 + (y - a\sin\ \phi)^2]^{1/2} \tag{A2}$$

where ρ_1 and ρ_2 are the distances from the point (x, y, z) to the intersections of the ring of foci $2a$ with the plane through (x, y, z) and the z-axis. The angle ϕ defines the orientation of this plane with respect to the xz-plane. The positive sign in η should be used if $z \geq 0$ and the negative sign if $z < 0$. The range in which coordinates are defined are: $0 \leq \xi \leq \infty$, $-1 \leq \eta \leq 1$, $0 \leq \phi \leq 2\pi$. The inverse transformation is:

$$x = a[(\xi^2+1)(1-\eta^2)]^{1/2}\cos\phi,$$
$$y = a[(\xi^2+1)(1-\eta^2)]^{1/2}\sin\phi, \quad z = a\xi\eta. \tag{A3}$$

In the prolate case (Fig. 1), the two foci lie on the revolution axis z perpendicular to the surface. The elongation parameter ξ_0 $(1 \leq \xi_0 \leq \infty)$ is defined through the long axis perpendicular to the surface $R_\mathrm{l} = 2a\xi_0$ and the short axis parallel to the surface $R_\mathrm{s} = 2a\sqrt{\xi_0^2-1}$. The spheroidal coordinates are given by:

$$\xi = \frac{\rho_1+\rho_2}{2a}, \quad \eta = \frac{\rho_1-\rho_2}{2a}, \quad \phi = \arctan\left(\frac{y}{x}\right) \tag{A4}$$

with

$$\rho_1 = [(z+a)^2 + x^2 + y^2]^{1/2}, \quad \rho_2 = [(z-a)^2 + x^2 + y^2]^{1/2}, \tag{A5}$$

where ρ_1 and ρ_2 are the distances of the point (x, y, z) to the two foci and ϕ describes the orientation of the plane through (x, y, z) and the z-axis with respect to the xz-plane. In this case, the coordinates are defined within the following ranges: $1 \leq \xi < \infty$, $-1 \leq \eta \leq 1$, $0 \leq \phi < 2\pi$, and the inverse transformation is:

$$x = a[(\xi^2-1)(1-\eta^2)]^{1/2}\cos\phi,$$
$$y = a[(\xi^2-1)(1-\eta^2)]^{1/2}\sin\phi,$$
$$z = a\xi\eta. \tag{A6}$$

For both the oblate and prolate cases, using $\xi_1 = d/a$, the boundaries between the various regions are defined by

the flowing relations :

$$\text{regions 1 and 3:} \quad \xi = \xi_0, \quad -1 \leq \eta \leq \pm\frac{\xi_1}{\xi_0}, \tag{A7a}$$

$$\text{regions 2 and 4:} \quad \xi = \xi_0, \quad \pm\frac{\xi_1}{\xi_0} \leq \eta \leq 1, \tag{A7b}$$

$$\text{regions 3 and 4:} \quad \eta = \pm\frac{\xi_1}{\xi}, \quad \xi_1(1) \leq \xi \leq \xi_0$$
$$\text{for an oblate (prolate) particle,} \tag{A7c}$$

$$\text{regions 1 and 2:} \quad \eta = \pm\frac{\xi_1}{\xi}, \quad \xi_0 \leq \xi < \infty. \tag{A7d}$$

The positive sign should be used in the case of an island and the negative sign in the case of a cap, to keep the ξ_1 parameter positive. The spheroidal coordinates of a point $P = (x, y, z)$ with respect to $\mathcal{O}'$ are found by noting that $x'^2 + y'^2 = x^2 + y^2$ and $z' = z \mp 2d$, so that:

$$\begin{aligned}
\xi'(\xi,\eta) &= \frac{1}{\sqrt{2}}\xi\Bigg\{1 + 4\frac{\xi_1^2}{\xi^2} - 4r\frac{\xi_1}{\xi}\eta - s\frac{\eta^2}{\xi^2} \\
&\quad + \Bigg[\left(1 + 4\frac{\xi_1^2}{\xi^2} - 4r\frac{\xi_1}{\xi}\eta - s\frac{\eta^2}{\xi^2}\right)^2 \\
&\quad + 4s\frac{1}{\xi^2}\left(2r\frac{\xi_1}{\xi} - \eta\right)^2\Bigg]^{1/2}\Bigg\}^{1/2} \\
\eta'(\xi,\eta) &= 2\frac{\xi'(\xi,\eta)}{\xi}\left(\eta - 2r\frac{\xi_1}{\xi}\right) \\
\phi' &= \phi
\end{aligned} \tag{A8a}$$

where $r = 1, -1$ in the island and cap cases, respectively, and $s = 1, -1$ in the oblate and prolate case, respectively.

Appendix B: The spheroidal multipolar expansion

The multipolar spheroidal functions, which describe the "radial" part of the solution to Laplace equation (2.3) are expressed in the following way, for oblate (hat) and prolate (tilde) coordinates:

$$\begin{aligned}
\widehat{X}_\ell^m(\xi,a) &= \mathrm{i}^{m-\ell}\frac{(\ell-m)!}{(2\ell+1)!!}a^\ell P_\ell^m(\mathrm{i}\xi), \\
\widehat{Z}_\ell^m(\xi,a) &= \mathrm{i}^{\ell+1}\frac{(2\ell+1)!!}{(\ell+m)!}a^{-\ell-1}Q_\ell^m(i\xi),
\end{aligned} \tag{B1a}$$

$$\begin{aligned}
\widetilde{X}_\ell^m(\xi,a) &= \mathrm{i}^m\frac{(\ell-m)!}{(2\ell-1)!!}a^\ell P_\ell^m(\xi), \\
\widetilde{Z}_\ell^m(\xi,a) &= \frac{(2\ell+1)!!}{(\ell+m)!}a^{-\ell-1}Q_\ell^m(\xi).
\end{aligned} \tag{B1b}$$

Here $(n)!! \equiv 1 \times 3 \times ... \times (n-2) \times n$ for n odd and $(n)!! \equiv 2 \times \times ... \times (n-2) \times n$ for n even, and by definition $(-1)!! \equiv 1$. The associated Legendre functions of degree ℓ and order m of the first (P_ℓ^m) and second kind (Q_ℓ^m) have been introduced [19]. They are defined through the classical formulae [19] ($m \geq 0$):

$$P_\ell^m(\mathrm{i}\xi) = (-1)^m \mathrm{i}^{\ell+m}\frac{(1+\xi^2)^{m/2}}{2^\ell \ell!}\left(\frac{\mathrm{d}}{\mathrm{d}\xi}\right)^{\ell+m}(1+\xi^2)^\ell, \tag{B2}$$

$$\begin{aligned}
Q_\ell^m(\mathrm{i}\xi) &= (-1)^{m+1}\mathrm{i}^{\ell+1}\frac{(1+\xi^2)^{m/2}}{2^\ell \ell!}\left(\frac{\mathrm{d}}{\mathrm{d}\xi}\right)^m \\
&\quad \times \Bigg\{2\left(\frac{\mathrm{d}}{\mathrm{d}\xi}\right)^\ell\left[\arctan(1/\xi)(1+\xi^2)^\ell\right] \\
&\quad - \arctan(1/\xi)\left(\frac{\mathrm{d}}{\mathrm{d}\xi}\right)^\ell(1+\xi^2)^\ell\Bigg\}.
\end{aligned} \tag{B3}$$

for the oblate case along the imaginary axis with $0 \leq \xi \leq \infty$ and by:

$$P_\ell^m(\xi) = (-\mathrm{i})^m\frac{(\xi^2-1)^{m/2}}{2^\ell \ell!}\left(\frac{\mathrm{d}}{\mathrm{d}\xi}\right)^{\ell+m}(\xi^2-1)^\ell, \tag{B4}$$

$$\begin{aligned}
Q_\ell^m(\xi) &= (-1)^m\frac{(\xi^2-1)^{m/2}}{2^\ell \ell!}\left(\frac{\mathrm{d}}{\mathrm{d}\xi}\right)^m \\
&\quad \times \Bigg\{\left(\frac{\mathrm{d}}{\mathrm{d}\xi}\right)^\ell\left[\ln\left(\frac{\xi+1}{\xi-1}\right)(\xi^2-1)^\ell\right] \\
&\quad - \frac{1}{2}\ln\left(\frac{\xi+1}{\xi-1}\right)\left(\frac{\mathrm{d}}{\mathrm{d}\xi}\right)^\ell(\xi^2-1)^\ell\Bigg\}
\end{aligned} \tag{B5}$$

for the prolate case along the real axis with $1 \leq \xi \leq \infty$. For $m < 0$ one should use the definitions:

$$\begin{aligned}
P_\ell^m(x) &= (-1)^m\frac{(\ell+m)!}{(\ell-m)!}P_\ell^{-m}(x), \\
Q_\ell^m(\xi) &= \frac{(\ell+m)!}{(\ell-m)!}Q_\ell^{-m}(x)
\end{aligned} \tag{B6}$$

with $x = \mathrm{i}\xi$, ξ, respectively, for the oblate and prolate case and with the appropriate limit for ξ. The associated Legendre functions of first or second kind and their derivatives for real or imaginary arguments $P_\ell^m(z)$ and $Q_\ell^m(z)$ (Eqs. (B2)–(B5)) are computed with the stable recurrence relations [19,37]:

$$F_\ell^m(z) = \frac{1}{\ell-m}\left[(2\ell-1)zF_{\ell-1}^m - (\ell-1+m)F_{\ell-2}^m\right], \tag{B7a}$$

$$\frac{\mathrm{d}F_\ell^m}{\mathrm{d}z}(z) = \frac{1}{z^2-1}\left[\ell z F_\ell^m - (\ell+m)F_{\ell-1}^m\right] \tag{B7b}$$

where F_ℓ^m stands for either P_ℓ^m or Q_ℓ^m and $z = x$ or $\mathrm{i}x$. The angular part of the Laplace equation (2.3) is included in the spherical harmonics $Y_\ell^m(\arccos\eta, \phi)$:

$$Y_\ell^m(\arccos\eta,\phi) = \left[\frac{2\ell+1}{4\pi}\frac{(\ell-m)!}{(\ell+m)!}\right]^{1/2}(-1)^m P_\ell^m(\eta)\mathrm{e}^{\mathrm{i}m\phi} \tag{B8}$$

$$C^m_{\ell\ell_1} = u_{21}\left(\frac{2\epsilon_1}{\epsilon_1+\epsilon_2}\right)\xi_0^{\ell_1+1}Z^m_{\ell_1}(\xi_0)\delta_{\ell\ell_1} - v\left(\frac{\epsilon_1-\epsilon_2}{\epsilon_1+\epsilon_2}\right)\zeta^m_{\ell\ell_1}\xi_0^{\ell_1+1}[Z^m_{\ell_1}(\xi_0)Q^m_{\ell\ell_1}(t_\mathrm{r}) - (-1)^{\ell_1+m}V^m_{\ell\ell_1}(\xi_0,t_\mathrm{r})] \quad \text{(C1a)}$$

$$D^m_{\ell\ell_1} = -u_{43}\left(\frac{2\epsilon_3}{\epsilon_3+\epsilon_4}\right)\xi_0^{-\ell_1}X^m_{\ell_1}(\xi_0)\delta_{\ell\ell_1} + v\left(\frac{\epsilon_3-\epsilon_4}{\epsilon_3+\epsilon_4}\right)\zeta^m_{\ell\ell_1}\xi_0^{-\ell_1}[X^m_{\ell_1}(\xi_0)Q^m_{\ell\ell_1}(t_\mathrm{r}) - (-1)^{\ell_1+m}W^m_{\ell\ell_1}(\xi_0,t_\mathrm{r})] \quad \text{(C1b)}$$

$$F^m_{\ell\ell_1} = \left(\frac{2\epsilon_1\epsilon_2}{\epsilon_1+\epsilon_2}\right)\xi_0^{\ell_1+2}\frac{\mathrm{d}Z^m_{\ell_1}(\xi_0)}{\mathrm{d}\xi_0}\delta_{\ell\ell_1} + vu_{21}\epsilon_1\left(\frac{\epsilon_1-\epsilon_2}{\epsilon_1+\epsilon_2}\right)\zeta^m_{\ell\ell_1}\xi_0^{\ell_1+2}\left[\frac{\mathrm{d}Z^m_{\ell_1}(\xi_0)}{\mathrm{d}\xi_0}Q^m_{\ell\ell_1}(t_\mathrm{r}) + (-1)^{\ell_1+m}\frac{\partial V^m_{\ell\ell_1}(\xi_0,t_\mathrm{r})}{\partial\xi_0}\right] \quad \text{(C1c)}$$

$$G^m_{\ell\ell_1} = -\left(\frac{2\epsilon_3\epsilon_4}{\epsilon_3+\epsilon_4}\right)\xi_0^{-\ell_1+1}\frac{\mathrm{d}X^m_{\ell_1}(\xi_0)}{\mathrm{d}\xi_0}\delta_{\ell\ell_1} - vu_{43}\epsilon_3\left(\frac{\epsilon_3-\epsilon_4}{\epsilon_3+\epsilon_4}\right)\xi_0^{-\ell_1+1}\zeta^m_{\ell\ell_1}\left[\frac{\mathrm{d}X^m_{\ell_1}(\xi_0)}{\mathrm{d}\xi_0}Q^m_{\ell\ell_1}(t_\mathrm{r}) + (-1)^{\ell_1+m}\frac{\partial W^m_{\ell\ell_1}(\xi_0,t_\mathrm{r})}{\partial\xi_0}\right] \quad \text{(C1d)}$$

where the Legendre function for real argument $-1 \leq \eta \leq 1$ is given by:

$$P^m_\ell(z) = \frac{(1-z^2)^{m/2}}{2^\ell \ell!}\left(\frac{\mathrm{d}}{\mathrm{d}z}\right)^{\ell+m}(z^2-1)^\ell. \quad \text{(B9)}$$

Again for $m < 0$, one uses the formula (B6). Of course, the oblate and prolate spheroidal functions have the same asymptotic behaviour for $\xi \to \infty$, *i.e.*

$$X^m_\ell(\xi,a) \simeq r^\ell, \quad \text{(B10a)}$$

$$Z^m_\ell(\xi,a) \simeq r^{-\ell-1} \quad \text{(B10b)}$$

where r stands for the distance from the centre of the ellipsoid. These limits (equivalent to the spherical case) are useful to determine the polarizability of the particle.

Appendix C: The matrix elements

C.1 Matrix system

In this appendix, the matrix elements of the linear system equations (2.12) are given. In order to allow for the treatment of both the oblate and prolate cases simultaneously, the generic functions X^m_ℓ and Z^m_ℓ are used. In explicit calculations they should be substituted for oblate spheroids by $\widetilde{X}^m_\ell$ and $\widetilde{Z}^m_\ell$ and by $\widehat{X}^m_\ell$ and $\widehat{Z}^m_\ell$ for the prolate case. The matrix elements of the linear system defined by equations (2.12) can then be written as:

See equations (C1a, C1b, C1c, C1d) above

with, for oblate islands: $u_{21} = u_{43} = v = 1$ and for oblate caps: $u_{21} = \epsilon_2/\epsilon_1$, $u_{43} = \epsilon_4/\epsilon_3$ and $v = (-1)^{\ell+\ell_1+1}$. Here the following abbreviations are introduced:

$$X^m_\ell(\xi) = X^m_\ell(\xi,a)a^{-\ell}, \quad Z^m_\ell(\xi) = Z^m_\ell(\xi,a)a^{\ell+1},$$
$$\zeta^m_{ll'} = \frac{1}{2}\sqrt{\frac{(2l+1)\,(2l'+1)\,(l-m)!\,(l'-m)!}{(l+m)!\,(l'+m)!}}\cdot \quad \text{(C2)}$$

The functions $Q^m_{\ell\ell_1}(t_\mathrm{r})$, $V^m_{\ell\ell_1}(\xi,t_\mathrm{r})$, $W^m_{\ell\ell_1}(\xi,t_\mathrm{r})$ that appear in the coefficients of the linear system are:

$$Q^m_{\ell\ell_1}(t_\mathrm{r}) = \int_{-1}^{t_\mathrm{r}} P^m_\ell(\eta)P^m_{\ell_1}(\eta)\mathrm{d}\eta \quad \text{(C3a)}$$

$$V^m_{\ell\ell_1}(\xi,t_\mathrm{r}) = \int_{-1}^{t_\mathrm{r}} P^m_\ell(\eta)P^m_{\ell_1}(\eta')Z^m_{\ell_1}(\xi')\mathrm{d}\eta \quad \text{(C3b)}$$

$$W^m_{\ell\ell_1}(\xi,t_\mathrm{r}) = \int_{-1}^{t_\mathrm{r}} P^m_\ell(\eta)P^m_{\ell_1}(\eta')X^m_{\ell_1}(\xi')\mathrm{d}\eta. \quad \text{(C3c)}$$

In the spherical limit, this formulae reduce to the truncated sphere model which has been analyzed previously [15].

The right hand side of the linear system, *i.e.* the source field, is expressed by (with $v = 1$ and $v = (-1)^{\ell+2}$ for the oblate island and cap, respectively):

$$H^0_\ell = \sqrt{4\pi/3}E_0\cos\theta_0\left\{u_{21}\frac{\epsilon_1}{\epsilon_2}\xi_0^{-1}X^0_1(\xi_0)\delta_{\ell1} + v\left(\frac{\epsilon_1-\epsilon_2}{\epsilon_2}\right)\times\left[\sqrt{3}t_\mathrm{r}\zeta^0_{\ell0}Q^0_{\ell0}(t_\mathrm{r}) - \xi_0^{-1}X^0_1(\xi_0)\zeta^0_{\ell1}Q^0_{\ell1}(t_\mathrm{r})\right]\right\} \quad \text{(C4a)}$$

$$J^0_\ell = \sqrt{4\pi/3}E_0\cos\theta_0\epsilon_1\frac{\mathrm{d}X^0_1(\xi_0)}{\mathrm{d}\xi_0}\delta_{\ell1} \quad \text{(C4b)}$$

$$H^1_\ell = -\sqrt{2\pi/3}E_0\sin\theta_0\xi_0^{-1}X^1_1(\xi_0)\delta_{\ell1} \quad \text{(C4c)}$$

$$J^1_\ell = -\sqrt{2\pi/3}E_0\sin\theta_0\frac{\mathrm{d}X^1_1(\xi_0)}{\mathrm{d}\xi_0}\times[u_{12}\epsilon_2\delta_{\ell1} + v(\epsilon_1-\epsilon_2)\zeta^1_{\ell1}Q^1_{\ell1}(t_\mathrm{r})]. \quad \text{(C4d)}$$

The integrals, equations (C3), which appear in the linear system are computed by the Quadpack integrator of Piessens [38,39]. It allows the use of Gauss-Kronrod quadrature with a globally adaptive integrator to reach the desired accuracy. It handles well the strong oscillations of the integrand brought by the Legendre functions of high degree. The linear system, equations (2.12), is solved by the LU-decomposition scheme of Lapack [40,39]. For the ill-conditioned matrix system, a multiple precision algorithm based on the routines of Smith's ZM package [39,41] has been set-up. All the remaining calculations were performed in double precision.

C.2 The potential constant term ψ_0

Sometimes, it is useful to have a complete map of the potential around the island to see how vibrates the charge

on the cluster. In the expansion of the potentials, only one constant remains unknown namely ψ_0. The equation $\ell = 0$ of the linear system allows to determine this quantity through H_0^0 in terms of the others multipole coefficients. The result is:

$$\begin{aligned}\psi_0 = R_\perp \left(\frac{\epsilon_1}{\epsilon_2} - 1\right) \Bigg\{ & \frac{1}{\sqrt{3}} \zeta_{01}^0 Q_{01}^0 (t_\mathrm{r}) \\ & + t_\mathrm{r}[p - \zeta_{00}^0 Q_{00}^0 (t_\mathrm{r})] \Bigg\} E_0 \cos\theta_0 \\ & - \frac{1}{2\sqrt{\pi}} \sum_{\ell=1}^{\infty} A_{\ell 0} R_\perp^{-\ell-1} q \left(\frac{\epsilon_1 - \epsilon_2}{\epsilon_1 + \epsilon_2}\right) \zeta_{0\ell}^0 \xi_0^{\ell+1} \\ & \times [Z_\ell^0(\xi_0) Q_{0\ell}^0 (t_\mathrm{r}) - (-1)^\ell V_{0\ell}^0 (\xi_0, t_\mathrm{r})] \\ & + \frac{1}{2\sqrt{\pi}} \sum_{\ell=1}^{\infty} B_{\ell 0} R_\perp^{\ell} q \left(\frac{\epsilon_3 - \epsilon_4}{\epsilon_3 + \epsilon_4}\right) \zeta_{0\ell}^0 \xi_0^{-\ell} \\ & \times [X_\ell^0(\xi_0) Q_{0\ell}^0 (t_\mathrm{r}) - (-1)^\ell W_{0\ell}^0 (\xi_0, t_\mathrm{r})] \qquad \text{(C5)}\end{aligned}$$

with $p = q = 1$ for an island and $p = 0$, $q = (-1)^{\ell+1}$ for a cap. Notice that one must use either $\widehat{X}, \widehat{Z}, \widehat{V}, \widehat{W}$ functions with $R_\perp = R_\mathrm{s}$ or $\widetilde{X}, \widetilde{Z}, \widetilde{V}, \widetilde{W}$ with $R_\perp = R_l$ for oblate and prolate particles, respectively.

References

1. U. Kreibig, M. Vollmer. *Optical Properties of Metal Clusters*, Vol. 25 (Springer Verlag, Berlin, Germany, 1995).
2. R. Lazzari, J. Jupille, Y. Borensztein, Appl. Surf. Sci. **142**, 451 (1999).
3. D. Martin, J. Jupille, Y. Borensztein, Surf. Sci. **377-379**, 985 (1997).
4. D. Martin, F. Creuzet, J. Jupille, Y. Borensztein, P. Gadenne, Surf. Sci. **377-379**, 958 (1997).
5. T. Yamaguchi, S. Yoshida, A. Kinbara, Thin Solid Films **18**, 63 (1973).
6. T. Yamaguchi, S. Yoshida, A. Kinbara, Thin Solid Films **21**, 173 (1974).
7. D. Bedeaux, J. Vlieger, *Optical Properties of Surfaces* (Imperial College Press, London 2001).
8. D. Bedeaux, J. Vlieger, Physica A **67**, 55 (1973).
9. D. Bedeaux, J. Vlieger, Physica **73**, 287 (1973).
10. D. Bedeaux, J. Vlieger, Physica A **82**, 221 (1976).
11. J. Vlieger, D. Bedeaux, Thin Solid Films **69**, 107 (1980).
12. D. Bedeaux, J. Vlieger, Thin Solid Films **102**, 265 (1983).
13. A. Bagchi, R.G. Barrera, R. Del Sole, Phys. Rev. B **20**, 4824 (1979).
14. J. Lekner, *Theory of Reflection* (Martinius Nijhoff, Dordrecht, The Netherlands, 1987).
15. I. Simonsen, R. Lazzari, J. Jupille, S. Roux, Phys. Rev. B **61**, 7722 (2000).
16. M.M. Wind, J. Vlieger, Physica A **141**, 33 (1987).
17. M.M. Wind, J. Vlieger, Physica A **143**, 164 (1987).
18. T.C. Campbell, Surf. Sci. Rep. **27**, 1 (1997).
19. P.M. Morse, H. Feshbach, *Methods of Theoretical Physics*, Part. 1 and 2 (New-York, 1953).
20. J.D. Jackson, *Classical Electrodynamics* (Wiley & Sons, New York, 1975).
21. E.D. Palik, *Handbook of Optical Constants of Solids*, Vols. 1–2 (Academic Press, 1985).
22. H. Hövel, S. Fritz, A. Hilger, U. Kreibig, M. Vollmer, Phys. Rev. B **48**, 18178 (1993).
23. P.A. Bobbert, J. Vlieger, Physica A **147**, 115 (1987).
24. C.F. Bohren, D.R. Huffman, *Absorption and Scattering of Light by Small Particles* (John Wiley & Sons, New York, 1983).
25. C. Beita, Y. Borensztein, R. Lazzari, J. Nieto, R.G. Barrera, Phys. Rev. B **60**, 6018 (1999).
26. C.E. Román-Velázquez, C. Noguez, R.G. Barrera, Phys. Rev. B **61**, 10427 (2000).
27. T. Wenzel, J. Bosbach, F. Stietz, F. Träger, Surf. Sci. **432**, 257 (1999).
28. V. Coustet, J. Jupille, Il Nuovo Cimento D **19**, 1657 (1997).
29. C. Noguez, R.G. Barrera, Phys. Rev. B **57**, 302 (1998).
30. M.T. Haarmans, D. Bedeaux, Thin Solid Films **224**, 117 (1993).
31. R. Lazzari, I. Simonsen, unpublished results.
32. Y. Borensztein, R. Alameh, M. Roy, Phys. Rev. B **50**, 1973 (1994).
33. P. Hadzel, T. Radonn, Vacuum **54**, 125 (1999).
34. R. Lazzari, J. Jupille, *Silver layers on oxide surfaces: morphology and optical properties*, Surf. Sci. **482-485**, 823 (2001).
35. G. Dehm, C. Scheu, M. Ruehle, R. Raj, Acta Mater. **46**, 759 (1998).
36. T. Suzuki, S. Hidhita, K. Oyoshi, R. Souda, Surf. Sci. **437**, 289 (1999).
37. W.H. Press, S.A. Teukolsky, W.T. Vetterling, B.P. Flannery, *Numerical Recipes in Fortran* (Cambridge University Press, 1992).
38. R. Piessens, E. deDoncker Kapenga, C. Uberhuber, D. Kahaner, Series Comput. Mathematics Vol. 1 (1983).
39. `http://www.netlib.org`.
40. E. Anderson, *Lapack: User's guide on* `http://netlib.org` (3d edn.) (1999).
41. D.M. Smith, Trans. Math. Softw. **17**, 273 (1991).